Annual Progress Report

NASA ROSES 2005 - NNH05ZDA001N-DECISION

Decision Support through Earth-Sun Science Research Results

for

NNA07CN14A: Oceanic Convective Weather Diagnosis and Nowcasting

Submitted by:

Cathy Kessinger, Huaqing Cai, Matthias Steiner, Nancy Rehak and Daniel Megenhardt
National Center for Atmospheric Research
Boulder, CO

Richard Bankert and Jeffrey Hawkins
Naval Research Laboratory
Monterey, CA

Earle Williams and Michael Donovan
Massachusetts Institute of Technology Lincoln Laboratory
Lexington, MA

15 November 2008

Table of Contents

List of Tables

List of Figures

Executive Summary (NCAR)

Few, if any, high resolution, weather products exist today that depict the current and future location of oceanic convection and associated hazards such as turbulence, icing and lightning. Federal Aviation Administration (FAA) projections suggest that the capacity growth rate for U.S. commercial air carriers within international markets will average 5.2% per year between 2010-2025 (FAA 2008). Likewise, revenue passenger miles (RPM) are forecast to increase an average of 5.2% per year while enplanements are forecast to increase an average of 4.6% per year during this same period. With this expected increase in international air traffic and passenger volume, an even greater need exists for high resolution, weather products for the oceanic aviation community. Currently, operational, international significant meteorological information (SIGMETs) statements are issued every four hours for convection, turbulence and icing over domains of such large extent that aircraft on oceanic routes must traverse, rather than avoid, the domain. Oceanic regions present unique challenges for weather product development due the scarcity of meteorological observations and the necessary reliance on satellite observations as a primary means of weather depiction.

In this project, we address the needs of the oceanic aviation community through the development of oceanic convective diagnosis and nowcasting products that are based on geostationary and polar-orbiting satellite data and global numerical model fields. These products are available in real-time through a web-based display and are in alignment with the concept of the four-dimensional weather data cube envisioned by the Joint Program Development Office (JPDO) Next Generation Air Traffic System (NextGen).

Annual Progress Report
Oceanic Convective Weather Diagnosis and Nowcasting

1. Introduction (NCAR)

This report summarizes the accomplishments of the National Center for Atmospheric Research (NCAR), the Naval Research Laboratory (NRL) and the Massachusetts Institute of Technology (MIT) Lincoln Laboratory (LL) for the National Aeronautics and Space Administration (NASA) Research Opportunities in Space and Earth Sciences 2005 (ROSES 2005; NNH05ZDA001N-DECISION) award for the proposal entitled "Oceanic Convective Weather Diagnosis and Nowcasting (NNA07CN14A)". This collaborative group is developing convective detection and nowcasting products for use by the oceanic aviation community by providing 0-hr, 1-hr and 2-hr nowcasts of convection location. This 3-yr ROSES grant was preceded by a 1-yr NASA Cooperative Agreement Notice (CAN) NNH04ZYO010C for a proposal entitled "Oceanic Convective Weather Diagnosis and Nowcasting (NNS06AA22G)".

During Year 1 of this ROSES grant and the 1-yr CAN grant (Kessinger et al., 2007), efforts were focused on the development of the software engineering infrastructure required for ingesting NASA mission products into the Convective Nowcasting Oceanic (CNO) system. The greater Gulf of Mexico domain (including the Caribbean, western Atlantic and eastern Pacific Oceans) has been the primary area of interest. Efforts were undertaken to ingest and apply quality control techniques to NASA mission products. Global Forecast System (GFS) model-based forecasting fields were described and their usefulness explained. The object-tracking methodology applied to extrapolate existing storms was initiated and examples compared to the 1-hr and 2-hr validation fields. The web site used for real-time display of products was also developed (http://www.rap.ucar.edu/projects/ocn).

In this Year 2 report, progress made on tasks is arranged into three topic areas: "Topics Related to the Convective Diagnosis Oceanic (CDO) Product", "Topics Related to the Convective Nowcasting Oceanic (CNO) Product" and "General Topics". Within the first topic, the case study of Hurricane Dean is described in Section 2 with the description of the CDO product given in Section 3. Efforts involved with validation of the CDO product against mission products from the Tropical Rainfall Measuring Mission (TRMM) satellite are described and results presented in Section 4. Further, efforts to upgrade the NRL Cloud Classification (CC) algorithm are described and results from a comparison to a second cloud typing algorithm are presented in Section 5. Within the second topic, Section 6 is a description of preliminary results for the characterization of the environment within which oceanic convection initiates to better understand potential forcing mechanisms. The CNO system, as currently configured, is validated in Section 7. Preliminary efforts to utilize a machine learning technique called Random Forest within the CNO are described in Section 8. Progress related to the inclusion of geostationary satellite-tracked wind fields into the extrapolation of CDO-identified storms is described in Section 9; quantifiable results are not yet completed to ascertain the effect that these winds may have to improve the statistical performance of extrapolation. Section 10 describes a brief study to examine the potential usefulness of the presence of African dust aerosols within the CNO system. For the third topic area, the addition of the near real-time North Atlantic cloud top height product to the project web pages (Section 11) is described, a summary and outlook for Year 3 (Section 12) is provided, and all journal and conference papers written during the year (Section 13) as well as all references used in this report are listed (Section 14).

Topics Related to the Convective Diagnosis Oceanic (CDO) Product

2. Case Study Selection (NCAR)

Hurricane Dean was the first land-falling Category 5 hurricane in the Atlantic basin since Hurricane Andrew in 1992 and was responsible for 32 fatalities. Dean traversed the Atlantic, Caribbean and Gulf of Mexico domains from 12-23 August 2007 (Figure 2.1). The National Hurricane Center Tropical Cyclone Report (Franklin, 2008) states that Dean formed from a tropical wave off the west coast of Africa on 11 August, became a tropical depression around 06 UTC on 13 August, and reached hurricane status early on 16 August about 480 n mi east of Barbados. By 19 August, Hurricane Dean was a Category 4 hurricane with a well-defined eyewall as seen by microwave and visible imagery (Figure 2.2). When Hurricane Dean made landfall on 21 August near the town of Majahual in the Yucatan Peninsula, Mexico, its central pressure was estimated at 905 mb with maximum sustained winds of 150 kt.

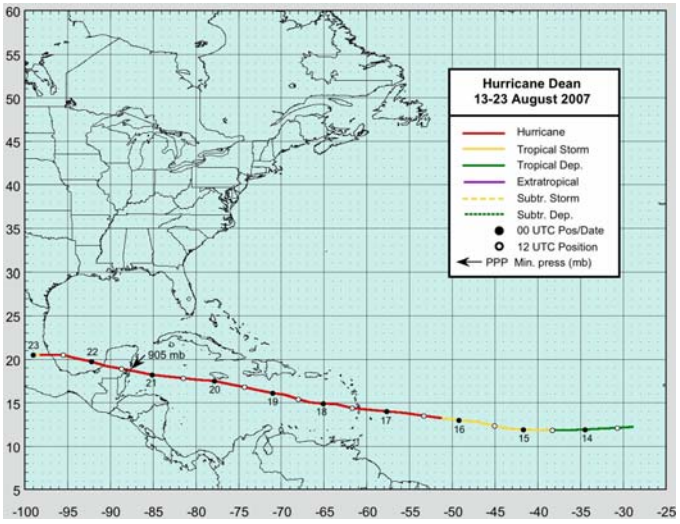

Figure 2.1. The best track positions of Hurricane Dean from 13-23 August 2007. Figure courtesy of Franklin (2008).

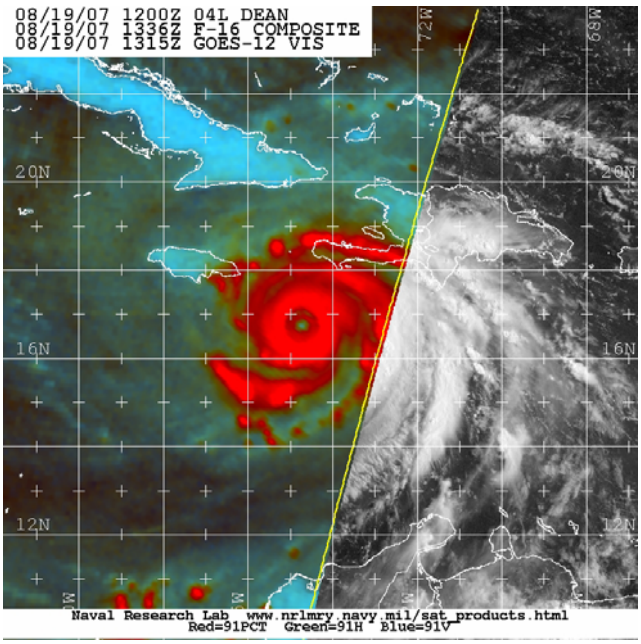

Figure 2.2. Microwave imagery of Hurricane Dean (1336 UTC) is superimposed over GOES-E visible imagery (1315 UTC) on 19 Aug 2007. Image was taken from the NRL Tropical Cyclone webpage at http://www.nrlmry.navy.mil/tc_pages/TC.html.

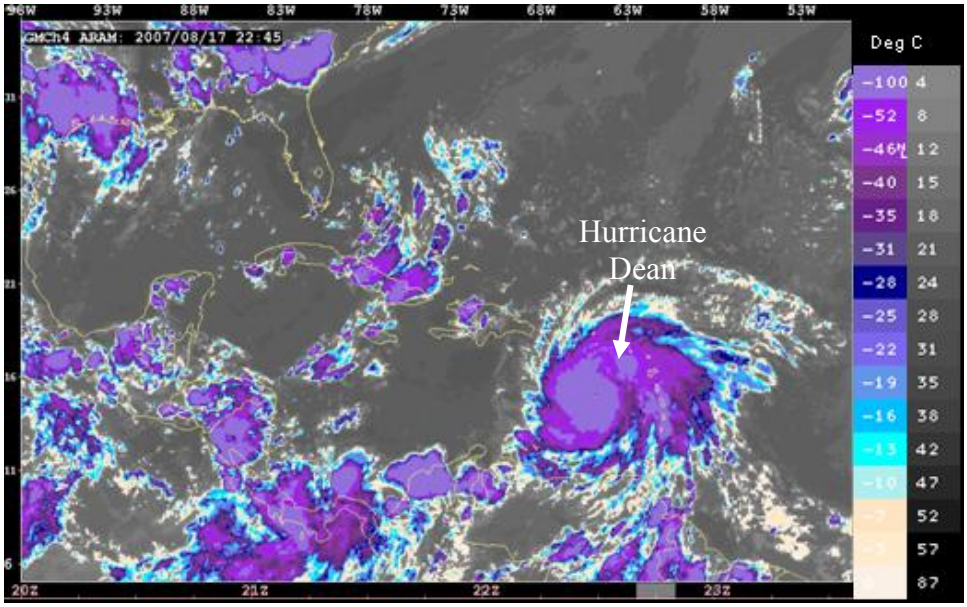

Figure 2.3. The longwave infrared satellite imagery is shown from GOES-East on 17 August 2007 at 2245 UTC. Hurricane Dean is indicated.

GOES-East infrared imagery on 17 August 2007 at 2245 UTC (Figure 2.3) shows the position of Hurricane Dean as well as significant amounts of convection over the CONUS, Cuba, Central America and northern South America. Purple-shaded regions define cloud top brightness temperature (BT) of -35^{o}C or less.

The time period covering Hurricane Dean is the foundation used for subsequent analysis of various tasks within this research effort. The validation of the CDO product using TRMM mission products is done over this period, as is the validation of the existing CNO product and the investigation into the Random Forest technique for CNO.

3. Description of the CDO product (NCAR, NRL)

The CDO algorithm developed at NCAR uses a fuzzy logic, data fusion technique on the outputs of three geostationary satellite-based algorithms that independently identify the location of deep convection (Kessinger et al. 2008) and is described here.

3.1. Component, diagnostic algorithms of the CDO

Convective clouds are identified via a fuzzy logic combination of three satellite-based algorithms called the Cloud Top Height (CTOP), the Cloud Classification (CC) and the Global Convective Diagnosis (GCD) to form the CDO product. The three algorithms are briefly described here and more fully in Donovan (2008).

Cloud Classification (CC) product: Using a supervised learning methodology that was first applied to AVHRR data (Tag et al. 2000), a cloud classifier was developed at the NRL with further refinements made for application to GOES data (Bankert and Wade, 2007; Bankert et al. 2008). A training data set is established through independent expert agreement of thousands of labeled 16*x*16 pixel samples. The classes used by the experts (and of relevance to this research) include cumulonimbus (Cb) and cirrostratus anvil (CsAn) for daytime classifications and a deep convection (DC) class at night. CsAn

represents relatively deep cirrostratus (Cs) near turrets in thunderstorms and is more closely related to deep convection than "garden variety" Cs. These four categories are inputs into the CDO product.

Each training set sample is represented by a vector of characteristic features computed or extracted from each spectral channel in the GOES imager. Various training sets were established, differentiated by satellite (GOES-East or GOES-West), sea or land, and day or night. A 1-nearest neighbor algorithm is used within the classifier. The minimum distance in feature space between an unclassified sample presented to the classifier and the training data samples is found and the class label of the nearest-neighbor training sample is subsequently assigned to each pixel in the unclassified sample.

Classifications of overlapping boxes (moving 16*x*16 pixel window) within each image are performed such that each image pixel is classified four times with the majority class assigned (ties broken randomly). Since each box is assigned a specific class, no "multiple", "overlapping", or "unknown" class is used.

Cloud Top Height (CTOP) product: The CTOP algorithm, developed at the NRL (Miller et al., 2005), combines geostationary longwave infrared (IR) channel data with the temperature profile data from the GFS model to estimate the heights of convective cloud tops over ocean and land surfaces during day- and night-time hours. For a given pixel location, the algorithm converts the satellite 11-μm IR brightness temperature (approximate cloud top temperature) to a cloud top height (pressure level) using the GFS vertical profile. The estimated pressure level is converted to height above sea level using the pressure vs. height relationship given by the standard atmosphere convention, which has been widely adopted for aviation use. Note that this algorithm is intended for use over deep cloud systems, not for cloud tops lower than 15K ft.

Global Convective Diagnosis (GCD) product: The GCD algorithm (Mosher 2002) computes, for a given pixel location, the brightness temperature (BT) difference between the water vapor channel (6.7-μm) and the longwave IR channel (11-μm). Deep, convective (i.e., optically thick) clouds that reach the tropopause are overlaid by dry, stratospheric air such that the BT of these two channels will be nearly equal at storm top. Within the GCD, near-zero differences (6.7-μm BT minus 11-μm BT) are associated with deep convection. The GCD, as devised by Mosher (2002), used the GFS 4-layer lifted index to remove thermodynamically stable regions. However, for the CDO product, this step was removed to prevent undesirable discontinuities resulting from the large grid spacing (0.5 degrees) of the GFS model.

3.2. CDO Methodology

The CDO product is computed using a fuzzy logic, data fusion procedure (Figure 3.1) that ingests output from the three algorithms discussed above and is described further in Kessinger (2008). Output from each of the three algorithms is scaled by a stepwise linear "membership function" such that values that positively indicate the desired feature (i.e., convective clouds) are scaled to unity while values that do not indicate the desired feature are scaled to zero (see Figure 3.1b-d). The output from the membership function scaling is termed an "interest (or likelihood) field". The interest outputs are weighted (GCD and CTOP use a weight of 1 while CC has a weight of 2) and summed to form the initial

CDO interest field with a maximum value of four during daytime and three at night due to the weighted contributions from the CC (Figure 3.1d). The final, binary CDO product is formed after the application of a threshold of 2.5 thus creating a binary indicator for the presence (=1) or absence (=0) of convection. The threshold value ensures positive contributions from at least two algorithms, whether day or night. Within this report, the term "CDO interest field" refers to the interest field where values vary between zero and four while the term "CDO product" refers to the binary, thresholded CDO field that is either zero or one.

The target audience for the CDO/CNO product suite is transoceanic, commercial aircraft that are flying at altitudes between 30-40 kft. Membership functions for the CDO component algorithms reflect this emphasis by the selection of categories for CC (Figure 3.1d), the scaling of higher cloud top levels in CTOP (Figure 3.1b) and the emphasis on deep convection by the GCD (Figure 3.1c). As the TRMM validation shows in the next section, warm rain clouds are typically not detected by the CDO due to their lower cloud top heights and warmer brightness temperatures as compared to deep convective clouds.

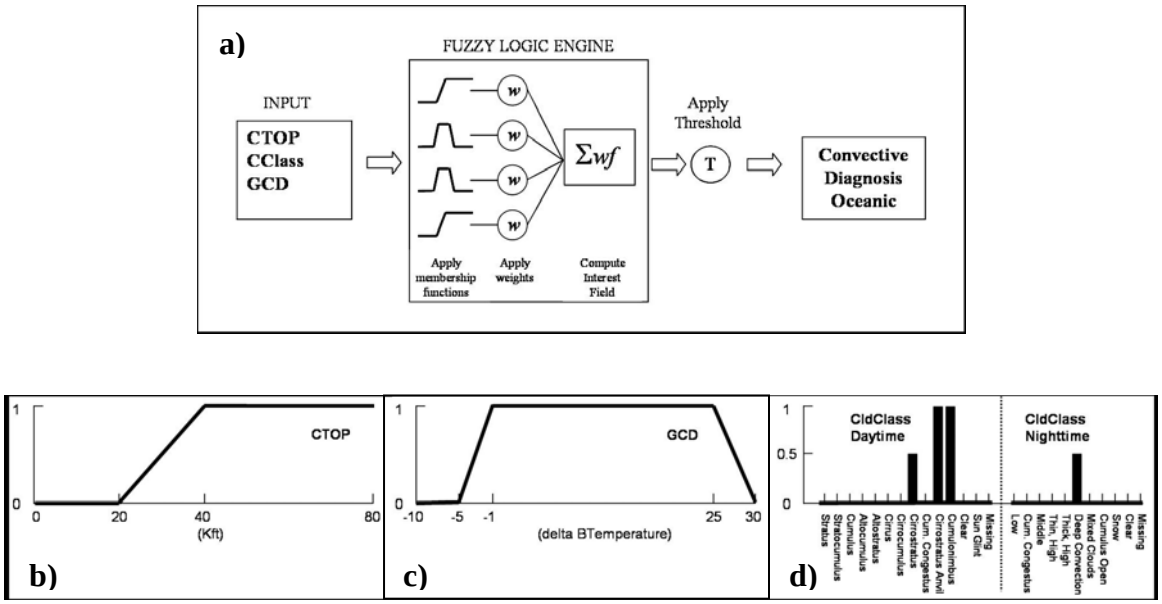

Figure 3.1. In a), a schematic shows the fuzzy logic, data fusion process used to calculate the Convective Diagnosis Oceanic (CDO) product. The membership functions for b) CTOP, for c) GCD and for d) CC are shown. Courtesy of Kessinger et al. (2008)

4. Verification of the CDO product using TRMM Observations (MIT LL)

4.1. Introduction

Following earlier methods used to intercompare the three independent convection diagnostic algorithms, this report describes how the CDO is validated against space-borne radar and lightning products from the TRMM satellite. A brief summary of what was learned in the previous intercomparisons is presented in Section 4.2. The methodology used to validate the performance of the CDO product and the verification results are

described in Sections 4.3 and 4.4, respectively. A summary and interpretation of the results follow in Section 4.5.

4.2. Earlier Verification Methods

Under sponsorship from the Federal Aviation Administration (FAA) Aviation Weather Research Program (AWRP), three intercomparisons of the convection diagnostic algorithms were performed over several years (Donovan et al, 2008). The duration, region of interest studied, and sophistication of each evaluation were subsequently improved. The first intercomparison entailed a study of the convection observed in the Gulf of Mexico for several hours during late morning and early afternoon for a single day in which convection was expected to develop. The algorithms were evaluated in their ability to detect large cloudy areas ($\geq$700 km^2) whose cloud top temperatures were very low ($\leq$230°K). Observations from the Tropical Rainfall Measuring Mission (TRMM) Lightning Imager Sensor (LIS) were used to distinguish thunderstorm clouds from cumulonimbus clouds that did not contain lightning.

Two regions were studied in the second intercomparison to compare algorithm performance over land (northern South America) and over the ocean (central Pacific Ocean). Similar to the first intercomparison, large cloudy areas containing cold cloud top temperatures (and presumed convective) were selected in the same manner for a duration of six days during the daylight hours. The TRMM Precipitation Radar (PR) data were introduced in this study in conjunction with LIS data to differentiate between cells presumed to be hazardous to aviation from non-hazardous cells and to evaluate the ability of each diagnostic algorithm to make such inferences.

A third intercomparison was the most comprehensive study. A large portion of the western Pacific Ocean served as the domain of interest. The duration of this study lasted nearly two months. Unlike the previous studies, cells were studied during the day and night at 3-hour intervals to coincide with the update rate of the GOES-9 full-disk satellite scans. The TRMM algorithm for precipitation type was introduced as an additional criterion for hazard.

Results from all three intercomparisons revealed that the diagnostic algorithms can achieve a 90% Probability of Detection (POD) rate of TRMM-verified hazardous cells when observed lightning is used as the criterion for hazardous status. However, each algorithm also showed a tendency to overestimate the presence of hazardous oceanic convection, a situation that could be improved through adjustments in thresholds for convection. These results are also likely due to shortcomings in the verification process. The horizontal resolution in the TRMM PR sampling and the modest time skew (~15 min) allowed between the GOES products and TRMM observations can impact the results during storm evolution. The fuzzy logic blending technique used in the CDO algorithm should help to improve performance compared to the outputs from each of the satellite-based algorithms for convection detection.

4.3. Verification Methodology of the CDO Interest

Current CDO interest field verification is consistent with the methodology implemented in the last (third) intercomparison. Throughout this section, the use of "CDO" refers to the CDO interest field that has not been thresholded to form the binary CDO product.

That is, the TRMM satellite observations from the LIS and PR are used to make inferences of whether clouds with cold cloud top temperatures are hazardous or non-hazardous to aviation. This designation is then compared with the CDO detection results to determine the algorithms' ability to discriminate hazardous convection. Several adjustments were made, however, to the rule set used in determining which cloud regions were selected for study and to the criteria used in determining whether a cloud is hazardous. These adjustments were deemed necessary because in the previous intercomparisons, large cloudy areas were treated mainly as a single event and the convection detection algorithms were scored accordingly. TRMM PR observations of these events often revealed the presence of discrete cores that depict regions of greatest updraft and turbulence (i.e., hazard) within a larger cloud region. Since these events were treated as a whole, the diagnostic algorithms were not penalized if their detected locations of convection did not match the hazard areas derived from TRMM data and consequently the amount of detection overestimation was not considered. Additionally, cloudy areas that showed no evidence of hazard by TRMM and were not diagnosed as convection by the CDO were not recorded in the evaluations, thereby eliminating an important scoring measurement, i.e., corrective negative. The geographical domain studied, the rule set for case selection, the criteria for hazard and the scoring rules were revised prior to the CDO verification.

The domain of interest selected to study the CDO interest performance consists of a large region encompassing the Gulf of Mexico, the Caribbean, and portions of the Atlantic and Pacific oceans. The red rectangle in Figure 4.1 illustrates the geographical location studied. The domain extends over 70 degrees of longitude from 30° W to 100° W and over 50 degrees of latitude from 35° N to −15° S. The large domain allows an evaluation of the CDO algorithm to detect continental convection over different land masses such as northern South America, southeastern United States and the Caribbean Islands. The domain also allows evaluation of maritime convection observed within large oceanic regions such as the Gulf of Mexico and portions of the western and central Atlantic Ocean. These regions were studied for a convectively active seven day period from 12-18 August 2007. The CDO interest data and TRMM data from all orbital overpasses within the domain were archived and translated onto a common grid with a spatial resolution of 6 km.

Figure 4.1. The red rectangle identifies the domain of interest where the verification of the CDO interest field was performed for the period 12-18 August 2007. The region of interest extends 70 degrees of longitude and 50 degrees of latitude.

Cases were selected for analysis if the visual inspection of the TRMM Visible and Infrared Radiometer (VIRS) observations revealed large cloudy regions ($\geq$216 km^2 or 6 grid bins) associated with contiguous cold cloud top temperatures (≤ -30°C) within the PR swath width (~243 km) and the TRMM and CDO interest data (based on GOES-12 satellite data) were time-coincident within 15 minutes. Special consideration was given to the temporal matching between the data sets, given the large size of the primary domain of interest. Each time-registered scan line of the TRMM orbital swath was compared to the estimated time of each scan line of the GOES-12 Northern Hemisphere extended sector at the latitudinal location being observed. All regions within the domain that were not time-coincident were excluded from the analysis. The temperature threshold was chosen to limit the evaluation to vertically developed clouds whose tops have reached high altitudes because the target audience of the CDO interest is for transoceanic commercial aircraft flying at altitudes between 30-40 kft, and because, on average, deeper clouds are characterized by stronger updrafts and generally more hazardous conditions.

For any cloudy region selected for analysis, the TRMM PR and LIS data were reviewed to determine whether conditions presumed hazardous to aviation exist. The PR reflectivity serves as an indicator of the stage of vertical development within deep convection and the LIS detects lightning activity that results from a vigorous updraft and an active mixed phase region of convection.

Three criteria were applied to each selected cloudy region to determine the presence of hazardous conditions:

1) The radar reflectivity at 5 km altitude (MSL), and the lower portion of the mixed phase region of convection, is $\geq$30 dBZ.

2) At least one lightning flash is detected in the cell of interest.

3) The NASA TRMM precipitation type algorithm classified the rainfall as ‘convective certain’ in regions where the IR brightness temperature ≤ -3°C.

If any combination of these three thresholds is exceeded, the hazard flag is raised for purposes of validation. If threshold (1) or (2) is exceeded the cell is considered hazardous; but if threshold (3) is the lone indicator of hazard, the cell is flagged as hazardous only if 5 or more grid bins (180 km^2 area) of convective rain are observed. To facilitate the CDO evaluation, a TRMM hazard product which identifies any combination of the criteria listed above is generated at the same 6 km spatial resolution and compared with the CDO interest data. For instances when the aerial extent of the cell’s cold cloud top temperature area (≤ -30 °C) of interest is spatially large (~ $\geq$2,500 km^2), the TRMM derived hazard product and the reflectivity observed at the 5 km altitude (CAPPI) are used to distinguish the cell as single or multiple events for purposes of scoring the CDO.

The scoring rules were also modified slightly. Large cloudy areas may be evaluated as a single or multiple event and correct negatives were recorded in order to compute additional categorical statistics, such as Accuracy, Bias, and Probability of False Detection (POFD), not computed in previous intercomparisons. In order to compute these statistics, a contingency table is created to record the frequency of ‘yes’

Table 4.1. CDO interest verification contingency table which shows the elements (in bold) necessary for computing several categorical statistics. The categories of 'yes' and 'no' TRMM hazard observed and the corresponding 'yes' and 'no' CDO detection are recorded for all cells selected for analysis.

Contingency Table				
		TRMM Hazard Observed		
		yes	no	total
CDO Detection	yes	***hit***	***false alarm***	*detect yes*
	no	***miss***	***correct negative***	*detect no*
	total	*hazard yes*	*hazard no*	*Total*

and 'no' CDO detections (using maximum interest value) against all 'yes' and 'no' TRMM hazard observations for each cloud cell that meets the selection criteria described above. Spatial tolerances between the CDO detection and TRMM hazard locations were allowed due to the temporal differences between the two data sets. Table 4.1 illustrates the elements within the contingency table that were recorded during the evaluation and is useful to identify the types of detection errors being made.

The table elements are defined as follows:

hit – TRMM observed hazard and CDO interest ≥ 2.5

miss – TRMM observed hazard and CDO interest < 2.5

false alarm – TRMM observed no hazard and CDO interest ≥ 2.5

correct negative – TRMM observed no hazard and CDO interest < 2.5

A perfect detection system would produce only *hits* and *correct negatives*, and no *misses* or *false alarms*. The statistics by category computed from these elements are presented in Section 4.4.

Figure 4.2 shows an example of the product analysis display used to evaluate visually the TRMM and CDO interest data for oceanic convection observed off the northeastern South American coastline at 14:26:44 UTC on 12 August 2007. The TRMM IR (Figure 4.2a) and PR reflectivity CAPPI at 5 km altitude (Figure 4.2b) are used to select cases for study and to identify single or multiple events within large cloudy regions. Note that generally the radar reflective areas are spatially well correlated with the IR areas, but are also generally smaller, in keeping with general experience. The radar is depicting the precipitating cores of convection, but in some cases is not present at all. The brighter white colors in Figure 4.2a represent IR cloud top temperatures ≤ -30 °C. The derived TRMM hazard product (Figure 4.2c) identifies hazard locations of significant elevated reflectivity (green), convective rain (blue) and lightning (red; none observed). The CDO interest field (Figure 4.2d) shows values ranging from 0-4. The light tan and red color keys represent CDO interest values ≥ 2.5 and designated regions of convection.

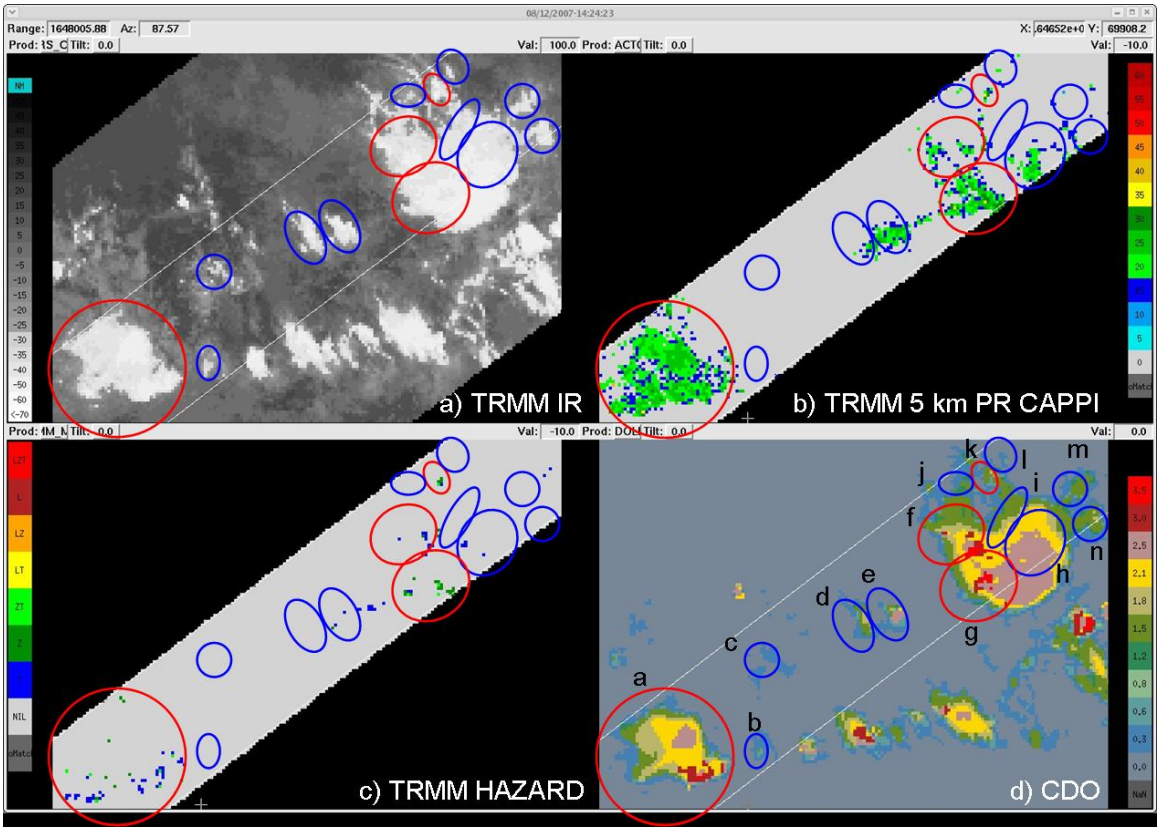

Figure 4.2. Four-panel analysis display showing the (a) TRMM IR (°C), (b) TRMM radar reflectivity (dBZ) at 5 km altitude, (c) TRMM derived hazard product, and (d) CDO interest field of oceanic convective clouds observed northeast of the South American coastline on 12 August 2007 at 14:26:44 UTC. The TRMM derived product denotes regions where our criteria for hazard was observed based on the following designations: T – convective rain, Z – reflectivity ≥30 dBZ at 5 km altitude, L – lightning, or ZT, LT, LZ, and LZT – combination of the hazard classes. An interest threshold of 2.5 is applied to the CDO interest field to indicate the presence of convective clouds. Distinctions between hazardous and non-hazardous cloud regions are indicated by red and blue ellipsoids, respectively. The TRMM PR swath width is 243 km.

The distinction made between the hazardous and non-hazardous cloud regions within the PR swath width (two white parallel lines) are shown as red and blue ellipsoids, respectively. Note the discrete reflectivity cores observed in the 5 km PR CAPPI (Figure 4.2b) are used to differentiate between single (Figure 4.2d, cell a) or multiple events (Figure 4.2d, cells f-i) in the two large cloudy regions. In this example, the CDO verification would yield 4 hits (a,f,g,k), 0 misses, 2 false alarms (e,h), and 8 correct negatives (b,c,d,i,j,l,m,n).

4.4. CDO Verification Results

Within the seven day period between 12-18 August 2007, 1,817 cells met the selection criteria for study and the frequency of 'yes' and 'no' CDO detection and TRMM observed hazard elements were recorded to complete the contingency table shown in Table 4.1. The elements within the Table were then used to compute several category

statistic scores such as POD, False Alarm Ratio (FAR), POFD, Accuracy, Bias, and Critical Success Index (CSI) to determine the performance of the CDO algorithm. The formula to compute each performance statistic and a brief definition are provided below.

POD = hits / (hits + misses)

(The fraction of the 'hazard yes' events correctly detected)

FAR = false alarms / (hits + false alarms)

(The fraction of the 'detect yes' events found to contain 'no' hazard)

POFD = false alarms / (correct negatives + false alarms)

(The fraction of the 'hazard no' events incorrectly detected as 'yes')

Accuracy = (hits + correct negatives) / total

(The fraction of the events correctly detected)

Bias = (hits + false alarms) / (hits + misses)

(The detection frequency of 'detect yes' events compared to the observed frequency of 'hazard yes' events)

CSI = hits / (hits + misses + false alarms)

(A measure of how well the detected 'hazard yes' events correspond to the observed 'yes' hazard events)

The element total and CDO statistical scores are provided in Table 4.2. The results of the verification were computed for all cells selected for analysis and further broken down into multiple categories (normalized) to compare CDO performance during the day and night, over ocean and land, for small and large cell spatial area, and for cells with and without observed lightning.

Regarding the 'all' category performance results, the CDO performed marginally well with a POD of 0.72, FAR of 0.26 and a CSI score of 0.58. The Bias score (0.98) indicates the CDO algorithm shows no tendency to under- or over-detect convective clouds. When comparing results for the other categories, there is no substantial difference in performance between the cells located over the ocean and over land. However, the CDO shows a considerable improvement in performance (POD, POFD, Bias and CSI) for cells observed during the daylight hours from those observed at night. Similarly, the CDO performance is much higher for the detection of large cells than for small cells. The last two categories delineate performance for all analyzed cells with or without observed lightning. The results indicate the CDO is much better at classifying clouds as convective if they contain lightning. The false alarm category and the remaining statistics cannot be tabulated for the lightning category because the CDO algorithm is not designed to detect this feature. The results in Table 4.2 are consistent with previous intercomparisons of the convection detection algorithms.

It should be noted that a small subset of cases (50, or 2.7% of all events) that were analyzed but excluded from the CDO verification statistics because they did not meet all the required criteria during the case selection process. In all instances, these cells were

Table 4.2. Detection performance statistics of the CDO algorithm for all hazardous and non-hazardous cells analyzed for the seven day period of 12-18 August 2007. The abbreviated column titles represent hits (H), misses (M), false alarms (FA), correct negatives (C Neg) and Accuracy (Acc).

CDO Verification Results										
Category	**H**	**M**	**FA**	**C Neg**	**POD**	**FAR**	**POFD**	**Acc**	**Bias**	**CSI**
all	613	237	216	751	0.72	0.26	0.22	0.75	0.98	0.58
day	502	112	172	1273	0.82	0.26	0.26	0.78	1.10	0.64
night	111	125	44	544	0.47	0.28	0.14	0.69	0.66	0.40
ocean	314	134	109	1036	0.70	0.26	0.19	0.77	0.94	0.56
land	299	103	107	781	0.74	0.26	0.28	0.73	1.01	0.59
small	143	124	51	701	0.54	0.26	0.12	0.75	0.73	0.45
large	470	113	165	1116	0.81	0.26	0.31	0.75	1.09	0.63
lightning	238	51	–	289	0.82	–	–	–	–	–
no lightning	375	186	216	1528	0.67	0.37	0.22	0.74	1.05	0.48

verified by TRMM to be hazardous by one or all hazard criterions but the size ($\geq$ 210 km^2 or 6 grid bins) and/or minimum IR cloud top temperature (≤ -30 °C) thresholds were not exceeded. Since these cells were likely in their early developmental stage, the CDO algorithm was given an allowance that it would likely not perform well or even 'see' these events owing to the fact that the time skew between the TRMM and GOES-12 satellite observations can be as great as 15 minutes. Owing to their compact nature, the hazard to aviation presented by these minority elements is deemed lower than normal.

The results in Table 4.2 were tabulated using a CDO interest detection threshold value of 2.5. In order to determine if the algorithm threshold is properly calibrated to achieve the best performance score, a sensitivity test was performed by computing the category statistics over a range of threshold values. The POD and POFD scores are then used to create a Relative Operating Characteristic (ROC) curve. The ROC measures the ability of the diagnostic algorithm to discriminate between convective and non-convective clouds. Figure 4.3 contains a plot of the ROC curve achieved by the CDO algorithm as the

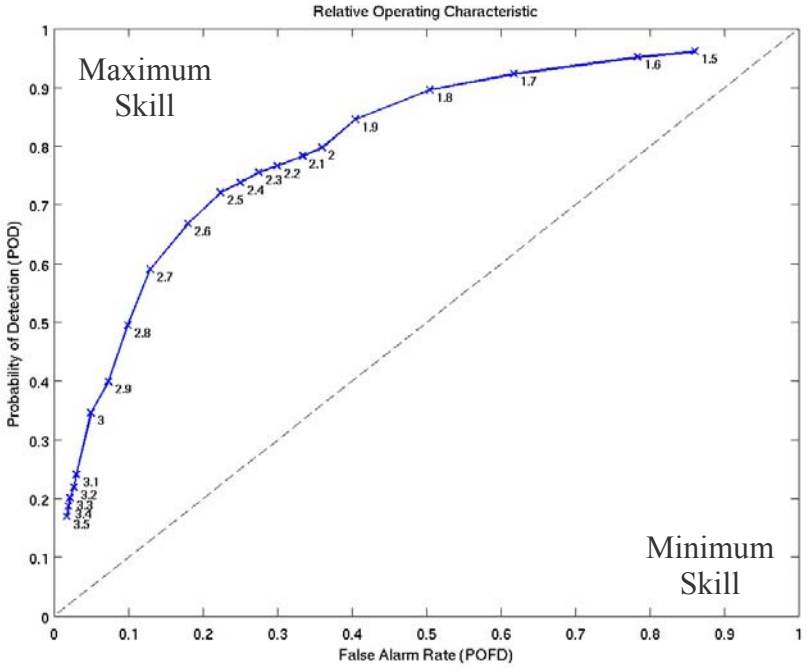

Figure 4.3. A plot of the False Alarm Rate (POFD) vs. the Probability of Detection (POD) achieved by the CDO algorithm for an interest threshold interval of 1.5–3.5. The interest value used to acquire the performance results shown along the curve are labeled next to each data point. The area under the curve and above the diagonal dashed line is often regarded as a score with the dashed line corresponding to the algorithm having no skill at discriminating between convective and non-convective clouds.

interest detection threshold value is adjusted from 1.5–3.5 at 0.1 interest intervals. Generally, the greater the area under the curve and above the dashed line is representative of higher algorithm performance. The curve endpoint interest threshold values of 1.5 and 3.5 indicate very poor algorithm performance is realized and yield a high POFD and low POD, respectively. As the threshold value is increased from 1.5, both the POFD and POD lower. The ROC curve in Figure 4.3 shows that the current interest threshold value (2.5) applied in the CDO algorithm yields the best performance. Categorical statistic scores were also computed for the same interest threshold range of 1.5-3.5 at intervals of 0.1. Figure 4.4 illustrates the CDO performance over this range for the same scoring metrics presented in Table 4.2. The results show that an interest threshold value of 2.5 produces the best CDO performance by achieving the highest Accuracy (0.75) and CSI (0.58) while maintaining the most neutral Bias (0.98). These results are consistent with the ROC curve results shown in Figure 4.3 and lend further confidence in the interest threshold currently used in the CDO algorithm.

An example of the CDO performance for mature Hurricane Dean located south of the Dominican Republic on 18 August 2007 at 13:44:11 UTC is illustrated in the four-panel analysis display in Figure 4.5. The TRMM IR (Figure 4.5a) and radar reflectivity at 5 km altitude (Figure 4.5b) show a broad area of very cold (≤−60 °C) IR brightness

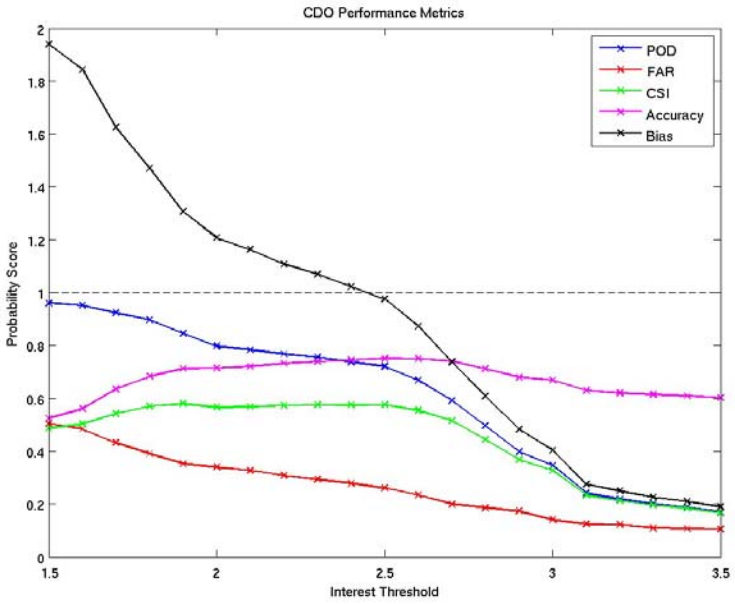

Figure 4.4. Plot of the CDO interest performance for several statistical categories over a range of interest threshold values of 1.5-3.5 at 0.1 intervals. The horizontal dashed line represents a perfect score for POD, CSI, and Accuracy and a neutral Bias score.

temperatures and significant rainfall, respectively. The TRMM derived hazard product (Figure 4.5c) shows substantial regions of hazard that coincide with the reflectivity observed at 5 km and additionally shows locations of hazard associated with LIS observed lightning (maroon and red colors) in the northeast eyewall and within the outer spiral bands. The CDO interest field (Figure 4.5d) does a very good job classifying a majority of this system as deep convection (regions $\geq$ 2.5) with the higher interest regions (maroon and red colors) matching well with the areas of coldest IR temperatures and strongest elevated reflectivity.

A cross sectional view of the TRMM radar reflectivity observed along the black solid line segment with end points A and B in each sub-panel plot is shown in Figure 4.6 along with the corresponding CDO interest values retrieved along this same path from the CDO grid in Figure 4.5d. The CDO interest values (shown at the top of the figure) are reported in color coded intervals to represent weak interest (blue – CDO<1.5), moderate interest (green – CDO$\geq$1.5 & <2.5), and high interest or detection of deep convection (red – CDO$\geq$2.5). It is interesting to note the most intense reflectivity cores, denoting the greatest vertical velocities within the hurricane, are being correctly classified as convection by the CDO. Even the small eye located at a range of ~520 km along the segment path, is depicted as a region of low interest by the CDO algorithm. The CDO values displayed at the top of Figure 4.6 are not spatially coincident and are shifted slightly left from the reflectivity cores observed by TRMM because GOES-12 scanned this region approximately 10 minutes after the TRMM orbit overpass. This time skew is allowed for during the CDO evaluation and the algorithm would not be penalized. Conversely, the CDO slightly overestimates the convection associated with the spiral band located at a range of 900 km along the segment path. The reflectivity core and derived hazard (Figure 4.5b,c) within this band is narrower than the CDO high interest region (Figure 4.5d).

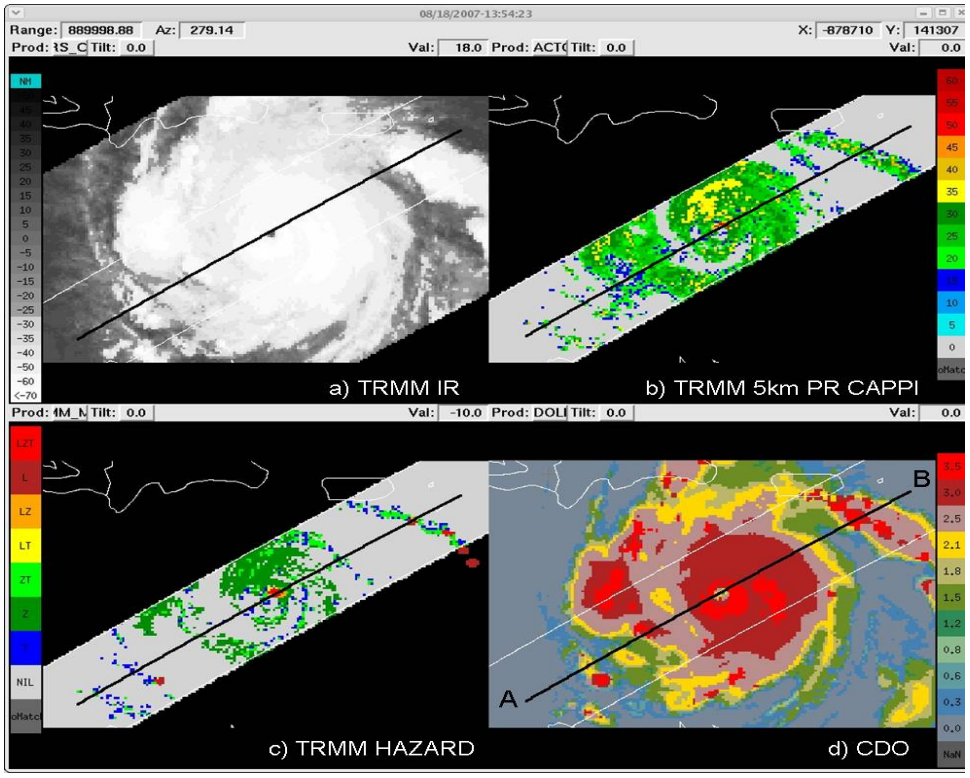

Figure 4.5. An example of the same four-panel display of products as shown in Figure 4.2 for convection associated with Hurricane Dean on 18 August 2007 at 13:44:11 UTC. A cross sectional view of the radar reflectivity and CDO interest values along the black line segment labeled A-B in (d) is illustrated in Figure 4.6. The TRMM PR swath width is 243 km.

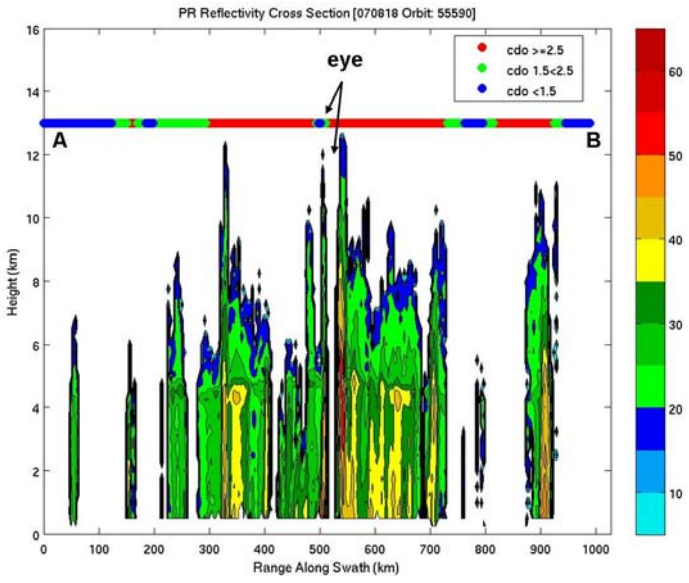

Figure 4.6 A cross section of the radar reflectivity (dBZ) associated with Hurricane Dean and observed by the TRMM PR along the A-B line segment shown in Figure 4.5d. The corresponding CDO interest values along this path are converted to color coded intervals defined in the legend box and represent regions of weak (blue), moderate (green) and strong (red) likelihood of convection. TRMM reflectivity ≥30 dBZ at the 5 km altitude is one criterion used to denote hazard.

A second example illustrating good CDO performance on several small cells located in the eastern Pacific Ocean west of Costa Rica is provided in the product plan-view analysis display in Figure 4.7 and the radar reflectivity cross section in Figure 4.8. The TRMM LIS did not detect lightning in these cells but the PR did detect significant discrete elevated reflectivity cores (Figure 4.7b) along with regions of convective rain signatures (Figure 4.7c). The CDO algorithm results shown in Figure 4.7d are mainly correct in designating all or a portion of these cloudy areas as convection. A comparison of the CDO interest values and the reflectivity cross-section along the A-B line segment is demonstrated in Figure 4.8. The taller and more developed cells centered at ranges 100 and 400 km along the segment path are denoted as convection by the CDO as is the shorter cell (likely in an early development stage) centered at 260 km. The CDO fails to detect the cell centered at 175 km but would not be scored as a 'miss' due to a time skew of 12 minutes between TRMM and GOES-12. This cell is classified as convection (interest $\geq$2.5) by the CDO in Figure 4.7d but the placement of the detection is shifted slightly north and west of the A-B line segment, likely due to the cell extrapolation that has occurred within the 12 minutes. Also, as noted in the previous example, the time skew between the satellite observations is the reason why the CDO interest values along the line segment A-B do match spatially (shifted left) with the reflectivity cores in Figure 4.8.

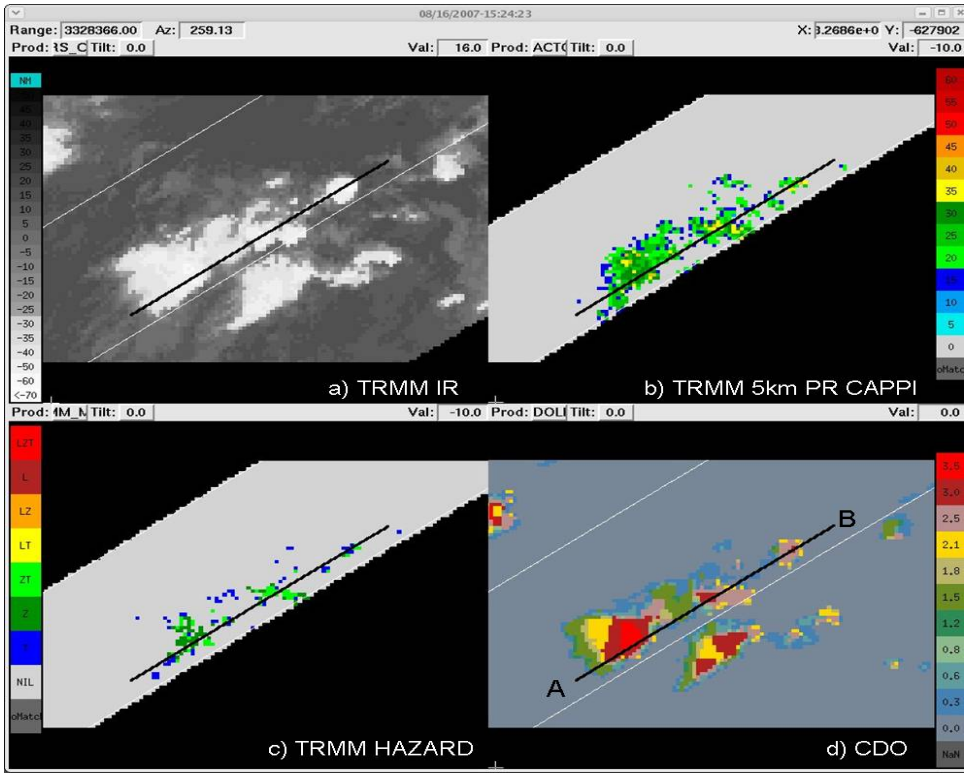

Figure 4.7. A second example of the same four-panel display of products as shown in Figure 4.2 for small cells located in the eastern Pacific Ocean on 16 August 2007 at 15:36:22 UTC. A cross sectional view of the radar reflectivity and CDO interest values along the black line segment labeled A-B in (d) is illustrated in Figure 4.8. The TRMM PR swath width is 243 km.

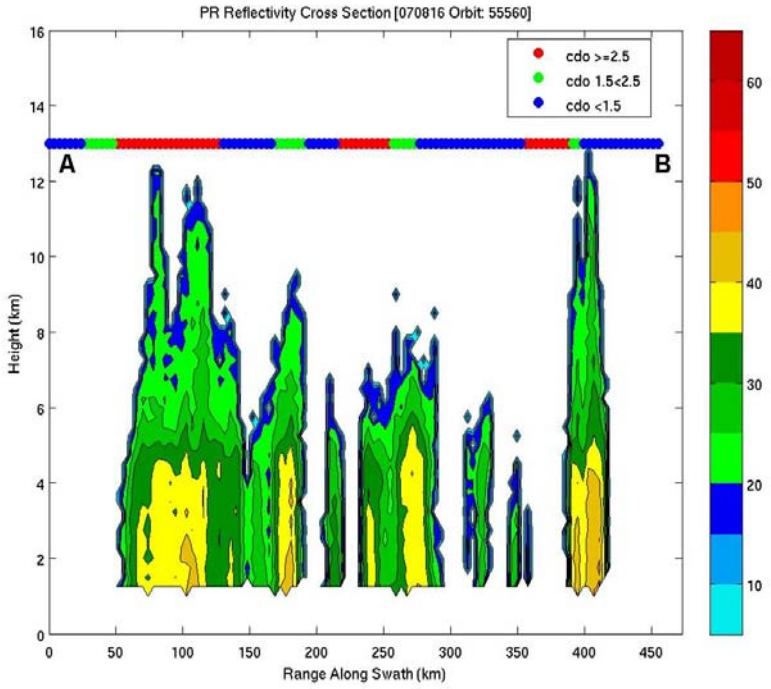

Figure 4.8. A cross section of the radar reflectivity (dBZ) for several cells observed by the TRMM PR along the A-B line segment shown in Figure 4.7d. The corresponding CDO interest values along the same path are shown at the top.

Figure 4.9 shows a third example of the TRMM products and CDO interest field for small and large cells observed over Cuba on 17 August 2008 at 22:54:09 UTC. Most of the smaller cells located over western Cuba contain narrow but well developed reflectivity cores and lightning (Figure 4.9c). The CDO interest field correctly designates these cells as convection. Within the two large cells centered over the island, small areas of weak elevated reflectivity ($\leq$25 dBZ) are observed and lightning is observed only within the southern portion of the large cell over eastern Cuba. The CDO in Figure 4.9d appears to overestimate the amount of convection (interest $\geq$2.5) in these two large cells, particularly the cell over central Cuba. A cross sectional view of the radar reflectivity along the line segment A-B is shown in Figure 4.10 and helps to explain why the CDO generated false detections. As mentioned above, the narrow and tall cell centered at 100 km range along the segment path is classified as hazardous by TRMM and detected as convection by the CDO. In the two large cells centered at range 270 and 480 km, most of the reflectivity is weak and located above the altitude of the mixed phase region and the altitude used to judge hazardous convection (5 km). The radar cross section gives the appearance that these cells were fully developed in the past but are now in the decaying stage of their life cycle. As a result, the CDO algorithm suffers from having no knowledge of cell evolution. It should also be pointed out that it is not known if elevated reflectivity of this magnitude (20-25 dBZ) produces turbulence or icing conditions hazardous to aviation. In the present study, these conditions are regarded as non-hazardous.

4.5. Summary and Interpretation

The verification results of the CDO algorithm using TRMM satellite radar and lightning observations indicate that a decent percentage (72%) of TRMM-verified hazardous cells

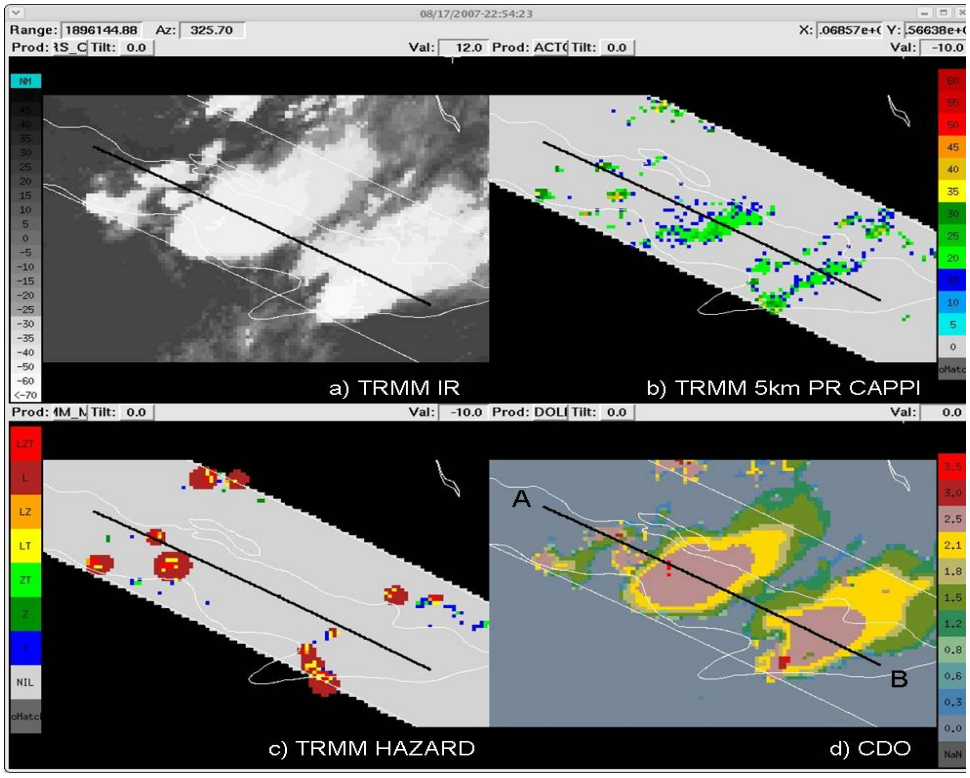

Figure 4.9. A third example of the same four-panel display of products shown in Figure 4.2 for cells located over Cuba on 17 August 2007 at 22:54:09 UTC. A cross sectional view of the radar reflectivity and CDO interest values along the black line segment labeled A-B in (d) is illustrated in Figure 4.10. The TRMM PR swath width is 243 km.

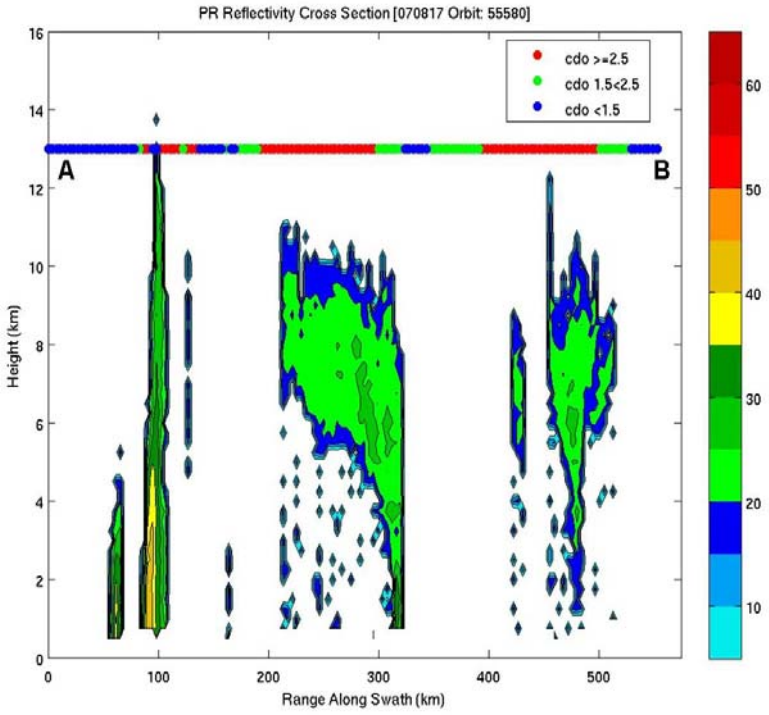

Figure 4.10. A cross section of the radar reflectivity (dBZ) for several cells observed by the TRMM PR along the A-B line segment shown in Figure 4.9d. The corresponding CDO interest values along the same path are shown at the top.

were classified as convection by the CDO. The FAR and CSI results were 26% and 58%, respectively. Given that the case selection criteria and verification methodology have changed significantly to incorporate smaller-sized cells and to measure algorithm skill at identifying the greatest hazard region within the cloud instead of treating the cell as a whole event, the composite product approach has demonstrated that the CDO algorithm is more skillful at identifying convection than the performance shown individually from the three convection detection algorithms in previous intercomparison studies (Donovan et al, 2008). The verification results have also given confidence that the current interest threshold (2.5) applied in the CDO algorithm produces the best performance with the least amount of bias (Figure 4.3 and Figure 4.4).

However, perfect algorithm detection in the presence of both imperfect algorithms and imperfect verification cannot be expected. The horizontal resolution of the TRMM PR (~5 km) can smear narrow reflectivity cores, and the time skew (~15 min) between geostationary satellite products and the TRMM observations can allow storm evolution to negatively impact the verification process. The analysis has shown a fundamental limitation in using satellite visible and IR information alone to make proper inferences about the internal characteristics of deep convective cells, specifically the hazards associated with updraft strength and turbulence. The CDO algorithm, based on the rather coarse IR features of the cloud veneer, typically detects the highest interest values near the cloud center and/or in regions containing the coldest cloud top temperatures as evident in Figure 4.2, Figure 4.5, and Figure 4.7. The TRMM observations, however, with their more detailed depiction of internal cloud structure, often exhibit the greatest hazard just as likely near the cloud cell edge and in regions warmer than the minimum cloud top temperature. In addition, cloud cells exhibiting very cold cloud top temperatures do not also equate to hazardous characteristics (Figure 4.9). This unfavorable result can be traced to a simple cause: a large number of oceanic cumulonimbus clouds attain high altitude ($\geq$40 kft) but lack a strong updraft (and attendant radar reflectivity aloft and lightning) (Donovan et al, 2008).

5. GOES Cloud Classifier Update (NRL, NCAR)

A long term goal for the NRL Cloud Classifier algorithm is to have the capability to run the algorithm within the computing environments of the Aviation Weather Center (AWC) and/or the National Weather Service (NWS). These agencies do not have access to satellite imagery stored in Terascan Data Format (TDF) but instead rely on the GOES Ingest and NOAAPORT Interface (GINI) and/or the McIDAS formats. A summary of efforts to achieve format independence is presented in Sections 5.2 and 5.3.

A secondary goal has been to increase the computational speed of the algorithm, thus allowing larger domains to be analyzed. Work was presented in last year's annual report (Kessinger et al, 2007) that summarized the effort to incorporate a reduced training set into the algorithm to reduce computational time. Testing of the reduced training set is underway as of this writing.

A third goal for the Cloud Classifier algorithm has been to run the algorithm using imagery from the MTSAT satellite. Preliminary results are shown in Section 5.4. This success puts the project in good form for expansion of the CDO/CNO products into the Pacific region, as planned for Year 3 of this proposal.

A general (not project specific) experiment to validate the Cloud Classifier through a comparison of outputs with an algorithm using a very different methodology is presented in Section 5.5. Discussion will include relevance of validation results to the CDO algorithm.

5.1. Background

As described in Section 3.1, the GOES Cloud Classifier (CC; Tag et al, 2000; Bankert and Wade, 2007) employs a 1-nearest neighbor algorithm to classify a specifically-sized sample (within an image) with the same cloud class as the training sample at the closest Euclidean distance in feature space. The characteristic features, extracted from the GOES channel data, define the feature space dimensions and are used to represent each training and testing sample. All pixels in a given test sample are assigned the same class. The classified sample boxes, in a given image, overlap each other such that each individual pixel is classified four times with the final classification determined by simple majority (ties broken randomly). Classes of interest for the CDO algorithm include cumulonimbus (Cb), high thick clouds associated with deep convection (CsAn), and cirrostratus (Cs) as classified in daytime imagery and deep convection (DC) at night.

5.2. Data format independence

The GOES CC algorithm was originally developed at the NRL where GOES data arrives and is processed using the Terascan environment. The classifier was, therefore, necessarily developed using the appropriate Terascan libraries and subroutines. Redesigning the classifier to run on any data format (Terascan, McIDAS, IDL, GINI, etc) has been completed to provide any potential user with a cloud classifier that only requires development of a "wrapper" to convert the data sets (in any initial data format) to binary files and then converting the classifier's binary output file to the data format of choice. The required input data sets and their associated properties that are used as input to the CC for GOES-11 and GOES-12 data are listed in Table 5.1.

After presenting these data sets to the classifier as binary data files, the classifier is run and the output file is binary with data type of byte. The dimensions (lines and samples) of both input and output data sets also need to be presented to the classifier. These dimensions along with the size of the domain determine the resolution of the data sets (input and output). An example of classifier outputs (displaying classes relative to the CDO) along with the images for the visible and longwave infrared (10.7 μm) channels are provided in Figure 5.1. There is good agreement between the TDF-dependent classifier output and the output from the classifier running binary data (original TDF data). The resolutions of the input (and output) data sets are very similar. Inputting binary data sets at or near 1-km resolution allows the classifier to produce classifications closer to the original design of the TDF-dependent classifier.

Table 5.1. Required input data sets (and their associated properties) for the GOES cloud classifier.

Data Set	Data Type	Units
Visible channel (0.65 μm)	byte	albedo*100
Near-IR chanel (3.9 μm)	float	degrees C
Water vapor channel (6.5 (GOES-12) or 6.7 μm (GOES-11))	float	degrees C
Longwave IR channel (10.7 μm)	float	degrees C
GOES-11 IR channel (12.0 μm)	float	degrees C
GOES-12 IR channel (13.3 μm)	float	degrees C
Land/Sea mask	byte	land=1; water=0
Latitude	float	degrees (-90.0 to +90.0)
Longitude	float	degrees (-180.0 to +180.0)
Solar zenith angle	float	degrees (angle)

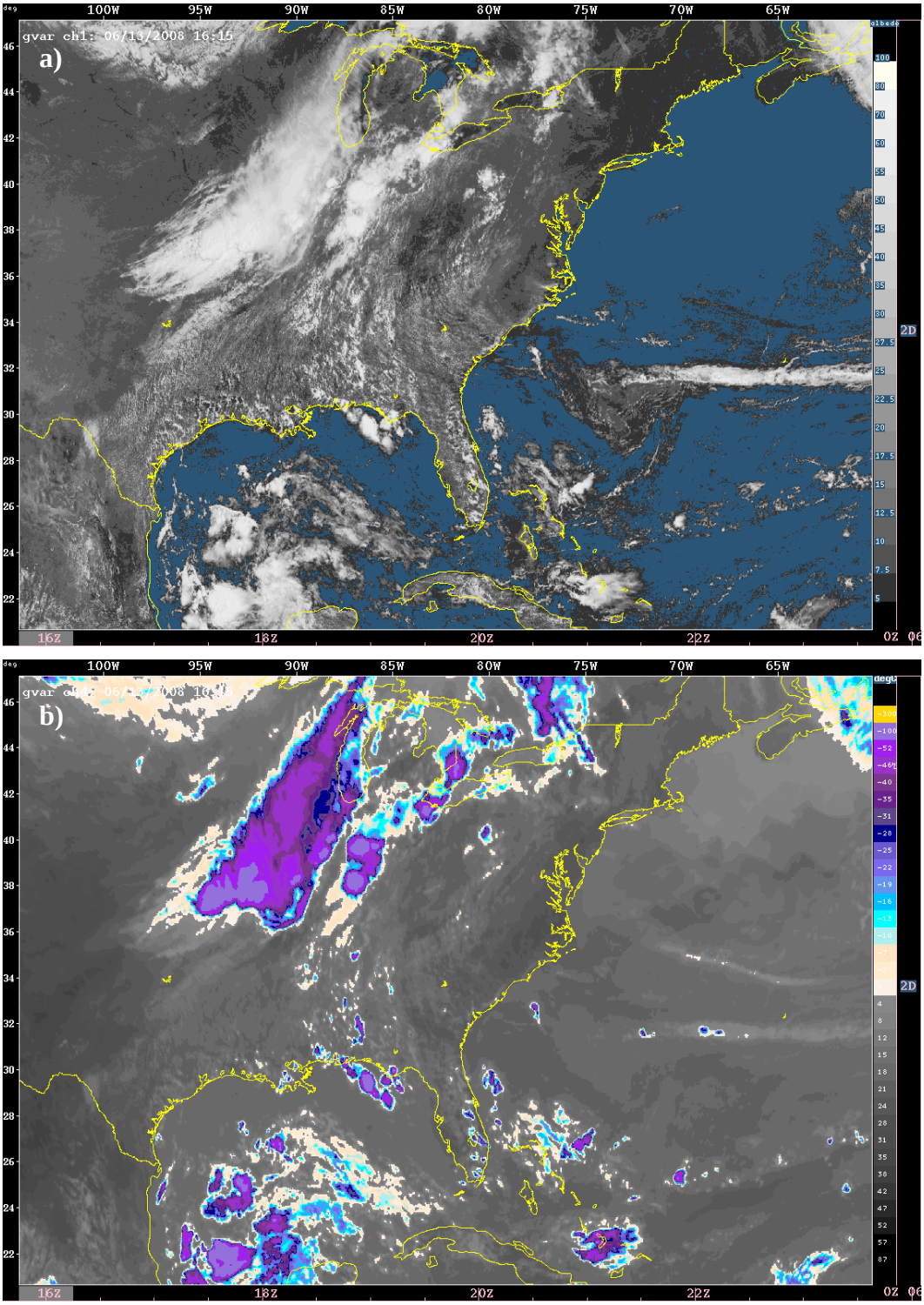

Figure 5.1. GOES-12 imagery and classification is shown over eastern U.S. and Gulf of Mexico for 13 June 2008 at 1615 UTC and includes: (a) visible channel and (b) longwave IR channel.

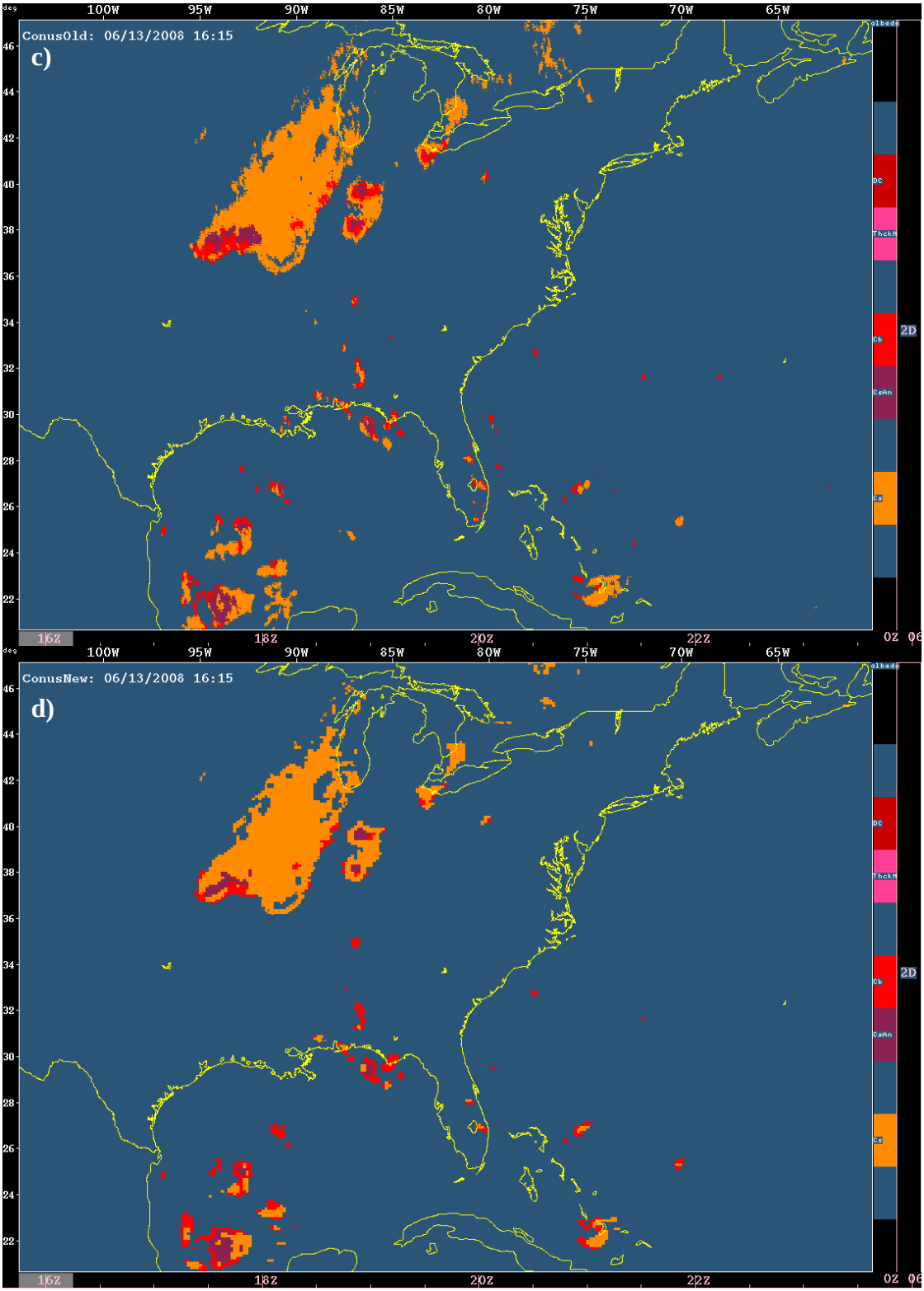

Figure 5.1, con't. GOES-12 imagery and classification is shown over eastern U.S. and Gulf of Mexico for 13 June 2008 at 1615 UTC and includes: (c) TDF-dependent classifier output (CDO classes only) and (d) data format independent classifier output (CDO classes only).

5.3. GINI data format

As stated above, a long term goal has been to port the CC algorithm to the NWS and the AWC for inclusion in thunderstorm nowcasting efforts as applied at the national and international levels. Because the algorithm was developed within the Terascan infrastructure, which is not available within NOAA, a re-engineering of the algorithm to remove data format dependencies was necessary to achieve this goal. The first technology transfer of the CC into the Advanced Weather Information Processing System (AWIPS) is now underway at the NWS Weather Forecasting Office (WFO) and the Center Weather Service Unit (CWSU) at Dallas, TX. The NWS funded the effort to ingest GINI format data while this ROSES grant funded the effort for format independence.

The NOAA agencies use the GINI format. The GINI imagery products (all channels) are broadcast as image (pixel) data and must be converted to the data units described in Table 5.1 prior to input into the CC. Further, the GINI data are only available over specific domains (which can have varying spatial resolutions) so its use within the CC is limited primarily to CONUS applications. Calculations for the land/sea mask, latitude/longitude and the solar zenith angle are not included in the GINI data and must be completed before input into the CC. An example classifier output (at the same date/time as Figure 5.1), using GINI data, is presented in Figure 5.2.

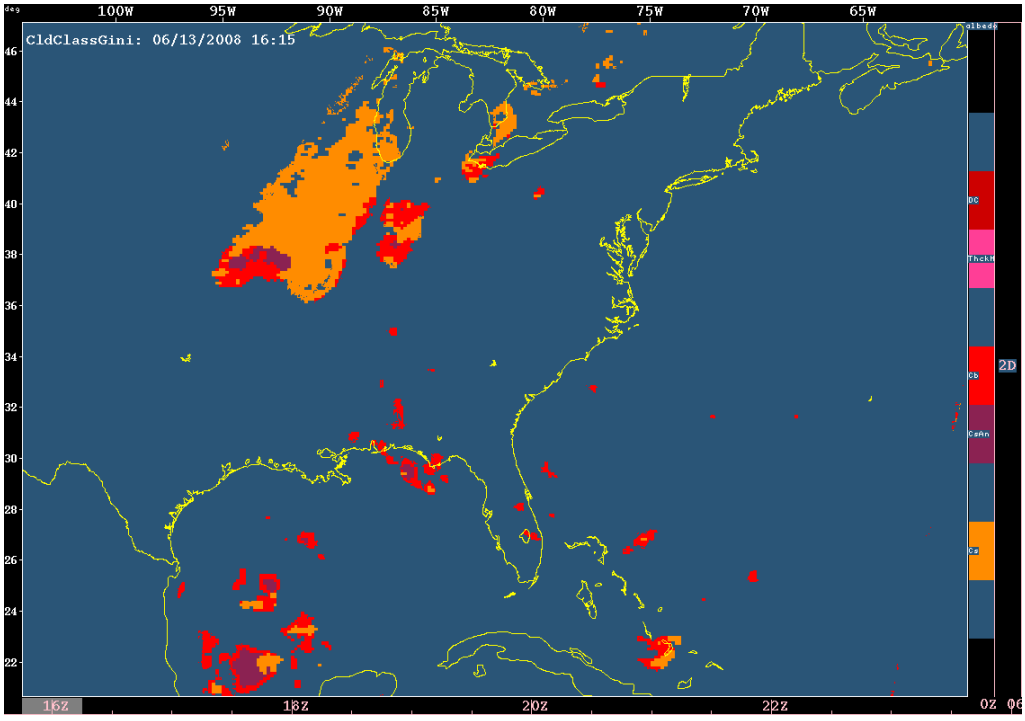

Figure 5.2. Classifier output (CDO classes only) using format-independent data (in this case GINI format) for the imagery in Figure 5.1.

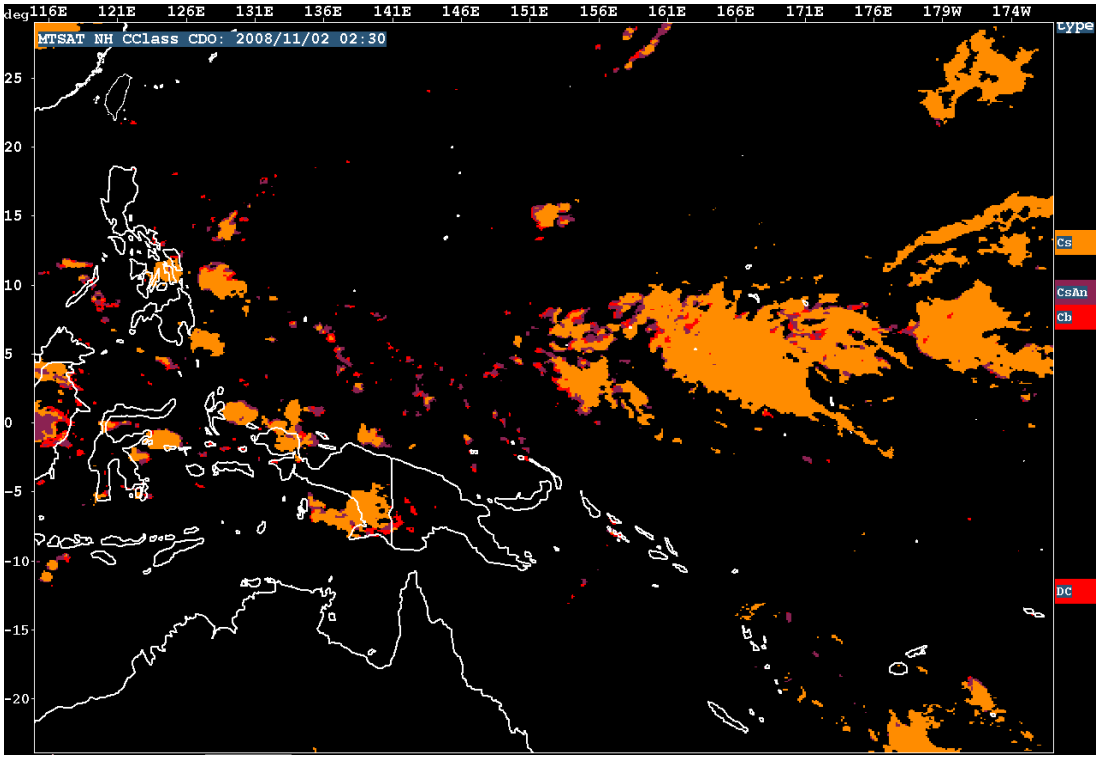

Figure 5.3. Preliminary results are shown from the CC algorithm using MTSAT-1R imagery as input for October 20, 2008 at 01:30 UTC.

5.4. Japanese Multi-Functional Transport Satellite (MTSAT-1R) imagery

To expand the oceanic domain over which the CDO/CNO system can be computed to the western Pacific Ocean, use of the Japanese MTSAT-1R is needed. The MTSAT-1R has the necessary channels to compute the CTOP and the GCD components of the CDO. To utilize the CC algorithm, a retraining and tuning exercise was required and initial results have been produced. The CC algorithm was initially run on MTSAT-1R imagery in the western Pacific with preliminary results shown in Figure 5.3 for the corresponding visible and infrared imagery (Figure 5.4). While these results appear consistent with results from GOES imagery, further work is required to validate the results. This effort will be undertaken in Year 3 of this proposal.

5.5. Validation experiment

Given the available data sets, a cloud classifier algorithm validation experiment was performed. The experiment and some results are discussed here as they are of interest to this project, given the CC usage within the CDO. With a lack of ground truth validation for each, output from two independently-developed GOES-11 cloud classifiers, one using implicit physics (used here within the CDO) and the other using explicit physics, are compared and analyzed. Results were presented in Bankert et al, (2008). Pixel-by-pixel comparisons, from a year of hourly daytime data in the NE Pacific (Figure 5.5), are analyzed. A high number of similar classifications for a given cloud class would bolster confidence in the individual classifier's output. While neither classifier can claim to be "ground truth", agreement between both classifiers – developed through very different methods – can give a user increased confidence in each classifier. Disagreements will

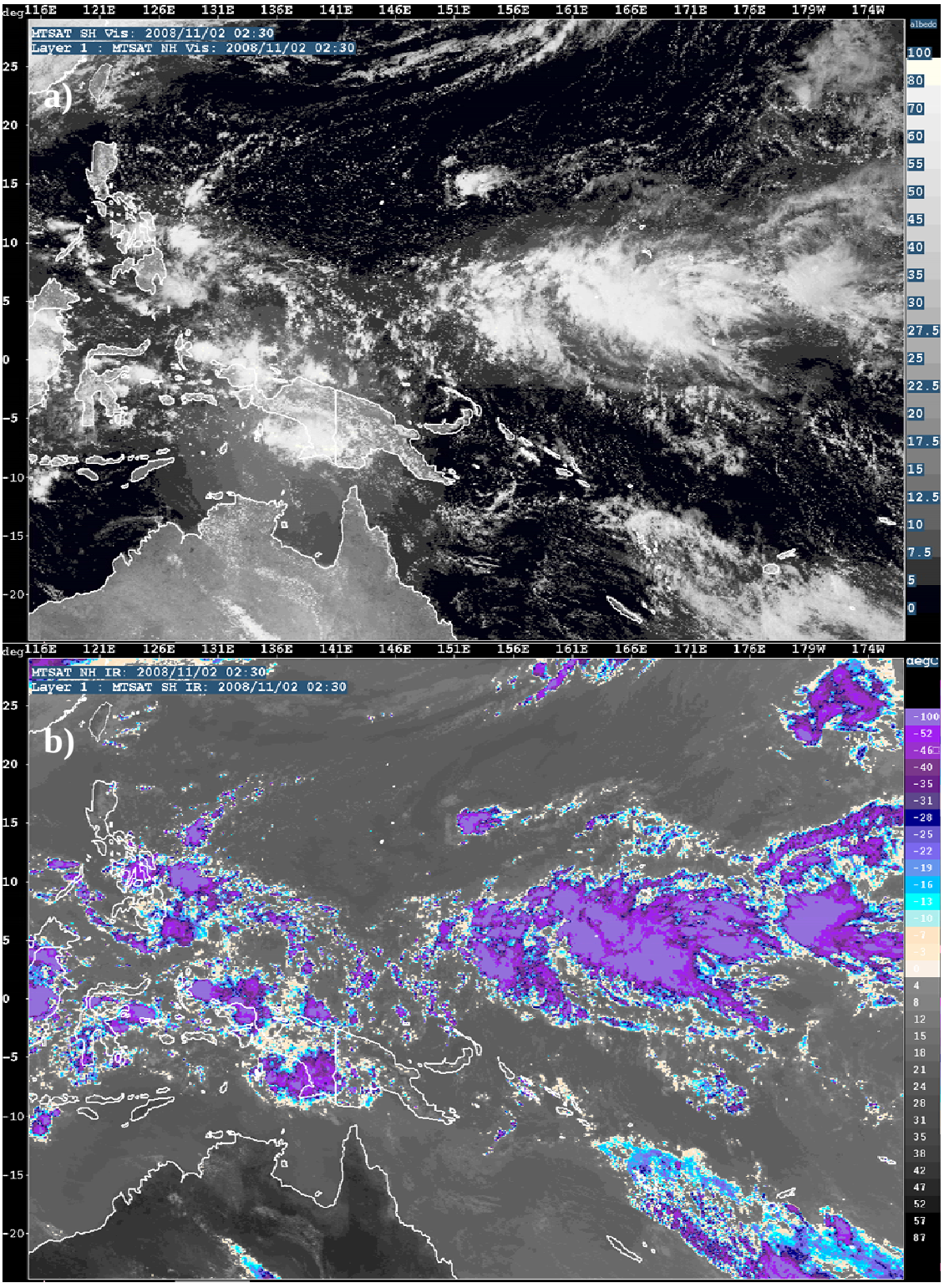

Figure 5.4. MTSAT-1 a) visible and b) longwave infrared imagery used as input into the CC algorithm (results shown in Figure 5.3) for October 20, 2008 at 01:30 UTC.

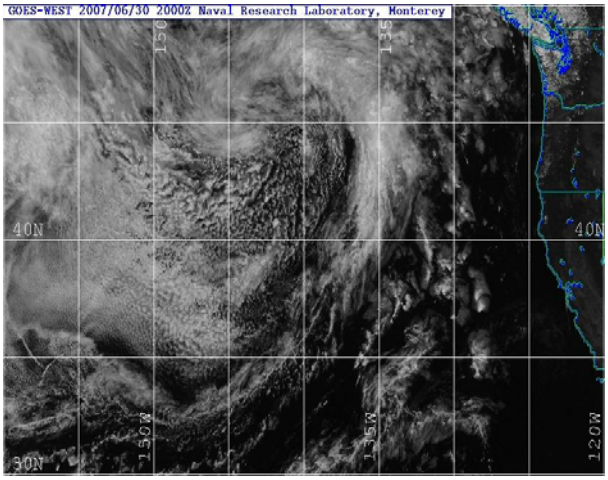

Figure 5.5. Area used for pixel-by-pixel comparison over a 1-yr period (GOES-11 visible image).

confirm or expose problem areas or limitations in one or both classifiers. Analysis of the disagreements may lead to classifier refinements or post-processing to improve the current classifications.

The GOES CC employs a supervised learning methodology (implicit physics) and is described in Sections 3.1 and 5.1 of the report. The daytime classes are listed in Table 5.2. For this experiment, pixels classified as Ground Snow, Haze, and Sunglint are ignored in the comparison analysis.

Table 5.2. Classes used in the NRL GOES cloud classifier (CC; "implicit physics").

Stratus (St)
Stratocumulus (Sc)
Cumulus (Cu)
Altocumulus (Ac)
Altostratus (As)
Cirrus (Ci)
Cirrocumulus (Cc)
Cirrostratus (Cs)
Cumulus Congestus (CuC)
Cumulonimbus (Cb)
CsAn (Cs near turret in thunderstorm; more closely related to deep convection than "garden variety" Cs)
Clear (Clr)
Ground Snow (Sn)
Haze (Hz)
Sunglint (Sg)

The "explicit physics" algorithm (CT) employed for this study is based on the works of Pavolonis, et al. (2005) and Pavolonis and Heidinger (2004). Using a series of thresholding and other thermal contrast, visible contrast, and spatial uniformity tests on the visible (0.65 μm), near-IR (3.9 μm), and longwave IR (11 μm) channels, each pixel is

assigned to one of the cloud types listed in Table 5.3. Partly cloudy types are ignored for this study.

Table 5.3. Cloud types used in "explicit physics" classification (CT) algorithm.

Clear (Clr)
Partly cloudy
Liquid water (Liq)
Supercooled water or Mixed phase (Mix)
Glaciated - opaque ice (Glac)
Cirrus (Ci)
Cloud overlap (OL)

A cloud mask algorithm first determines if a pixel is clear or cloud. For all pixels classified as cloud, the 11 μm channel brightness temperature is determined and an OL test and Ci test are applied. If both of these tests fail, the appropriate (based on 11 μm channel brightness temperature) cloud phase tests for liquid water, supercooled water or mixed phase, and glaciated (opaque ice) clouds are applied and the pixel's cloud type is assigned.

Hourly daytime data for each of the classifiers were collected over a one year time period (10/06 -10/07). In order to get a better one-to-one analysis when comparing the output of the two algorithms, the CC classes are combined to best match the CT cloud types. This clustering of classes is summarized in Table 5.4. Note there is no corresponding overlapping cloud class in the CC algorithm.

Pixel-by-pixel comparisons done over the entire year are summarized in the cloud class/type matrices displayed in Table 5.5 and Table 5.6. Table 5.5 gives the percent distribution within a specific CT type of how that cloud type was matched (pixel-by-pixel) with CC cloud classes (as described in Table 5.4). For example (marked in red), 57.2% of the pixels classified as mixed phase or supercooled water by the CT algorithm were classified as one of the liquid cloud classes by the CC algorithm. Table 5.6 gives the percent distribution within a CC class of how that cloud class was matched (pixel-by-pixel) with CT cloud types. Looking at the same table element described in the example above, 19.7% of the pixels classified as liquid cloud by the CC algorithm were classified as mixed phase or supercooled water by the CT algorithm.

There is much agreement between the two algorithms, especially in terms of clear pixels and liquid water cloud pixels. Confidence is increased in those cases where algorithms agree on the classifications. In addition, some of the disagreements may be a result of the different original sets of classes/types used as opposed to one (or both) of the classifiers being in actual error.

Many of the classifier disagreements are a result of the lack of an overlapping cloud class in the CC algorithm and/or missed OL classifications in the CT algorithm. As one example, since the CC algorithm does not have an OL class, actual OL pixels are classified as As or Ac with signals from both low cloud and overlying Ci being used to give a mixed phase classification. An example of this classification mixture can be seen

Table 5.4. CC class combinations used for comparisons with CT class types.

Liquid Water
Stratus (St)
Stratocumulus (Sc)
Cumulus (Cu)
Mixed phase / Supercooled water
Altocumulus (Ac)
Altostratus (As)
Cumulus Congestus (CuC)
Glaciated
Cirrocumulus (Cc)
Cirrostratus (Cs)
Cumulonimbus (Cb)
CsAn
Clear (Clr)
Cirrus (Ci)

Table 5.5. Percent (%) distribution of pixels within each CT algorithm type (columns) matched with CC class (rows) – columns sum to ~100%.

	Clr	Liq	Mix	Glac	Ci	OL
Clr	**94.0**	7.4	1.1	0.1	10.9	0.0
Liq	4.4	**89.5**	**57.2**	0.8	18.9	5.9
Mix	0.6	3.0	**31.3**	16.7	18.6	30.9
Glac	0.5	0.0	2.5	**74.9**	24.2	50.7
Ci	0.5	0.1	8.0	7.5	**27.3**	12.5

Table 5.6. Percent (%) distribution of pixels within each CC class (rows) matched with CT algorithm type (columns) – rows sum to ~100%.

	Clr	Liq	Mix	Glac	Ci	OL
Clr	**80.2**	11.5	0.8	0.0	7.5	0.0
Liq	1.9	**70.2**	**19.7**	0.1	6.5	1.6
Mix	0.8	7.6	**35.4**	7.0	21.1	28.0
Glac	0.6	0.0	2.6	**29.1**	25.4	42.3
Ci	1.4	0.4	16.4	5.7	**55.9**	20.3

within the front in Figure 5.6. High thin clouds are streaming across the low clouds associated with the front.

Adding OL samples to the CC training data, or establishing a post-processing check to determine if an overlapping cloud situation exists, would improve the CC classifier. Also, adjustment to the OL test in the CT algorithm, which is designed to minimize false alarms, would lower the frequency of misses by this classifier. Such adjustments may

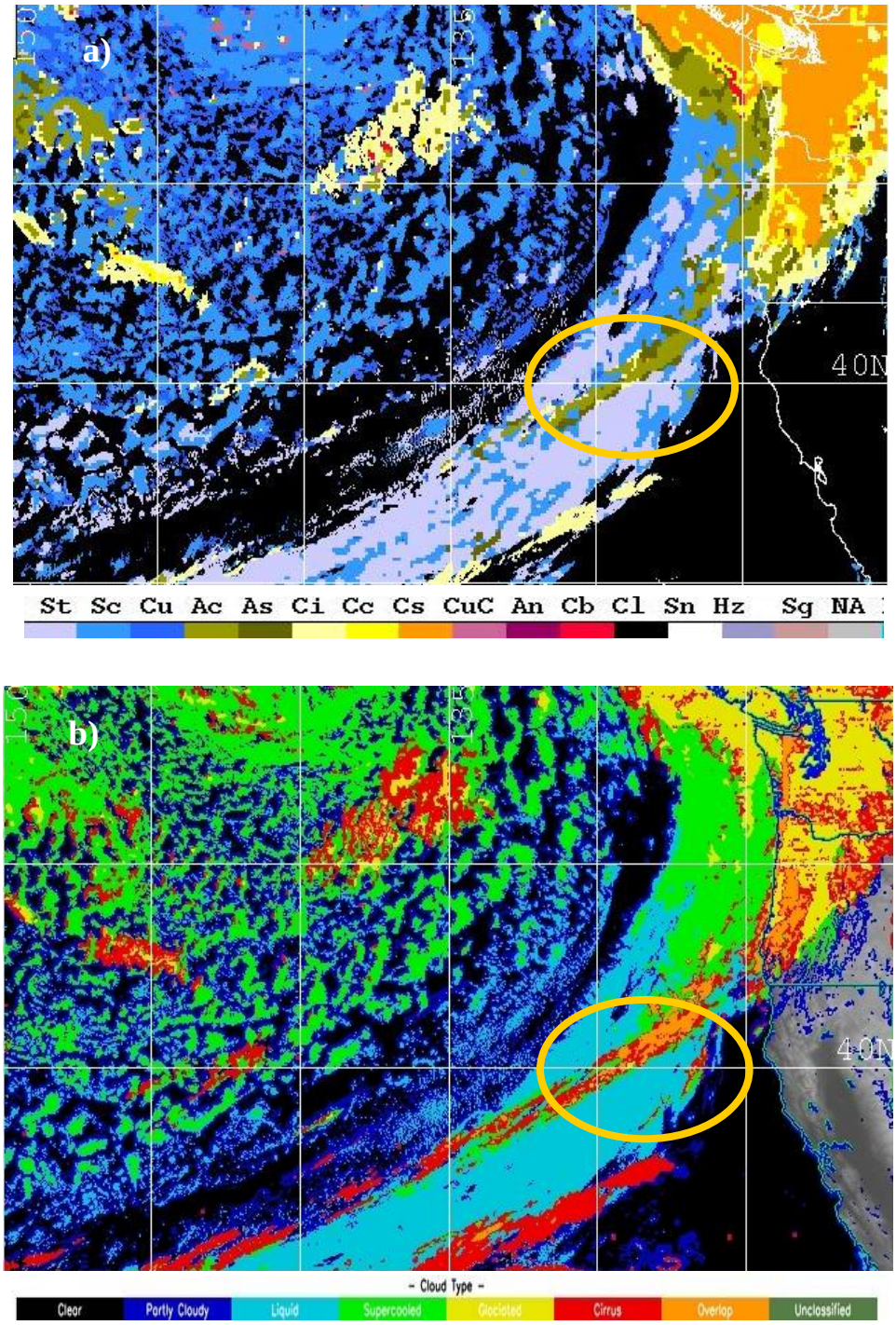

Figure 5.6. Example case (16 Apr 2007, 1700 UTC) of CC classification (a) of mid-level clouds (As or Ac) and the CT classification (b) of OL for the same pixels (area marked in gold oval).

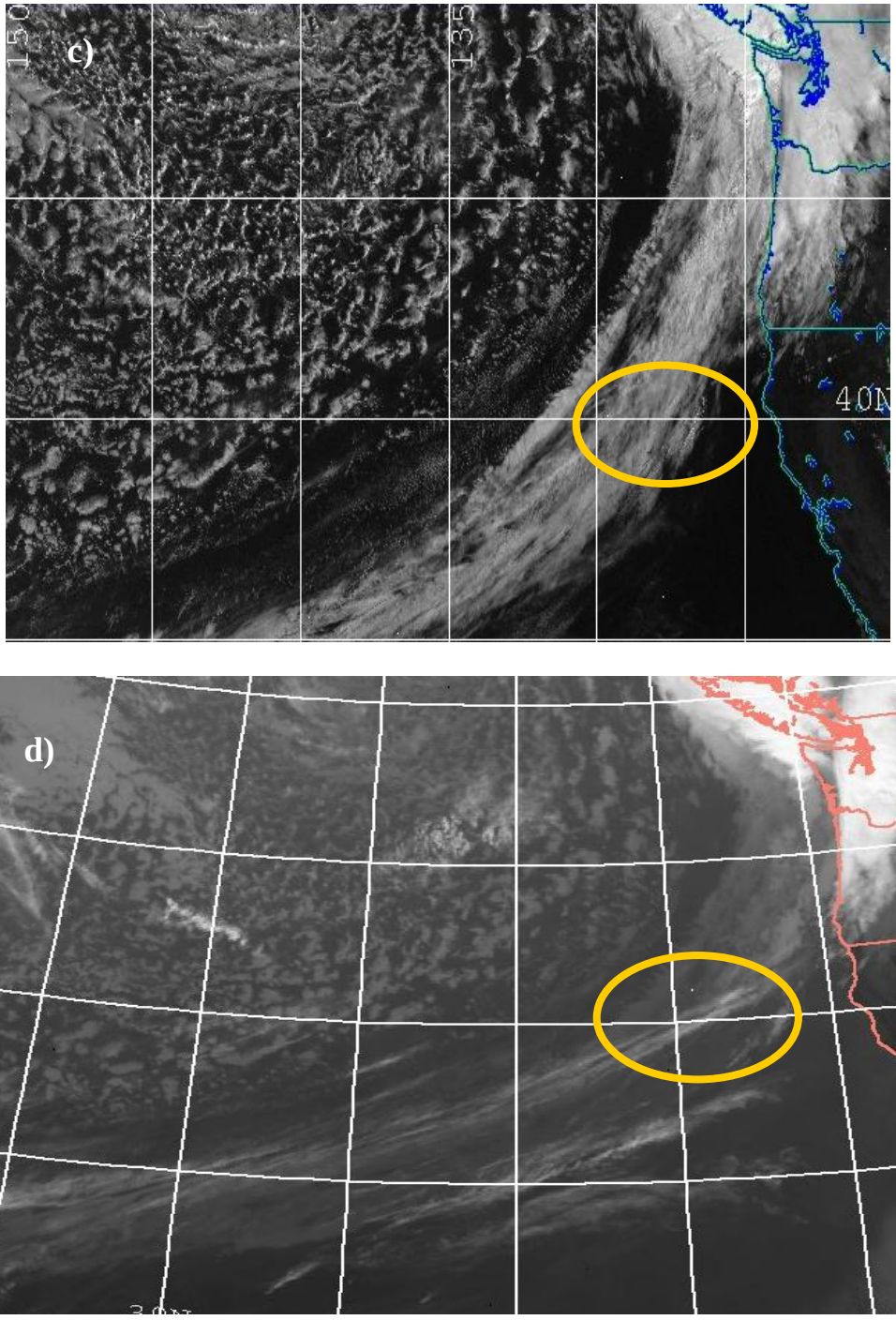

Figure 5.6, con't. Example case (16 Apr 2007, 1700 UTC) showing the GOES-11 visible (c) and longwave IR ((d) - different image projection) channels.

enlist other observing systems such as CloudSat, CALIPSO, or the 1.38 μm band on MODIS.

Relative to the CC classes used in the CDO, many of the disagreements occur when CC has a glaciated class (includes Cb and CsAn as well as Cs and Cc) and CT classifies the pixel as Ci or OL. These pixel classification disagreements are most likely the result of class definitions (particularly with regards to optical thickness for Ci), lack of an OL class in the CC algorithm, and classifier design rather than complete misclassifications. Interestingly, more pixels classified by the CC algorithm as Cs and Cc were paired with a CT classification of OL than Glaciated; whereas, pixels classified by the CC algorithm as Cb and CsAn had a higher frequency pairing with Glaciated than OL. These distributions are indicative of the optical thickness of the clouds as used indirectly in the class definitions and has given further confidence to the daytime classification provided by the CC algorithm to the CDO.

Neither the CC nor the CT algorithm can guarantee a completely accurate cloud-type representation for any given GOES data set. However, by using the output of each classifier, combined with knowledge of their reliability and limitations in certain situations, a final – more accurate - single classification product could be produced in certain situations and given user needs.

Topics Related to the Convective Nowcasting Oceanic Product

6. Examination of Environmental Characteristics versus Storm Initiation Location (NCAR)

6.1. Introduction

The importance of short-term forecasts for storm initiation has long been recognized by the aviation community; however, the skill to correctly forecast storm initiation remains poor, even over land where dense, surface-based observational networks are available. Over the ocean, storm initiation forecasts become even more challenging, owing to the lack of surface-based observational networks such as surface mesonets or the WSR-88D radar network. Recognizing the difficulty caused by the lack of surface-based observations, this study strives to utilize satellite-derived environmental parameters to identify favorable conditions for oceanic storm initiation.

The environmental fields being evaluated include the sea surface temperature (SST), near-surface convergence/divergence, Convective Available Potential Energy (CAPE), Convection Inhibition (CIN) and the atmospheric relative humidity. A simple scatter plot approach is employed to investigate the environmental conditions favorable for convection initiation (CI) over the ocean. The domain for this study is the Gulf of Mexico (see Figure 4.1 for domain area). The time period spans Aug 12 – 23, 2007 during the passage of Hurricane Dean (see Section 2). During this time period, convective activity was abundant through both initiation of new storms and through the advection of existing storms. Hurricane Dean was well-captured by the CDO algorithm.

6.2. Methodology

A simple scatter plot approach is employed to determine if the convective parameters under investigation serve as a good precursor of CI. CDO interest values contained within new convective storms, as represented by interest values >2.0, are plotted against various convective parameters to reveal potential relationships. Ideally, the full range of CDO interest values should be plotted (and will be at a later date) but, for this preliminary study, limiting the number of points was desired.

Storm initiation is determined by the first occurrence of a storm as defined by the Thunderstorm Identification, Tracking and Nowcasting (TITAN; Dixon and Wiener 1993) algorithm that is used to extrapolate/forecast the CDO product within the CNO. A minimum size criterion of 300 km^2 is used and a CDO interest threshold of $\geq$2.5 is applied to define a "new storm" per the CNO specifications. Using these TITAN-identified new storm polygons, the CDO interest field is thresholded to remove all storms except for the new ones. Then, scatter plots of the new storm CDO interest values versus various environmental convective parameters can be created. The CDO interest values (at each grid point) of the new storms are matched to the closest grid point of the environmental fields that occur within the hour previous to the new storm initiation time.

In the scatterplots below, the reader will notice that vertical lines of points accumulate at CDO interest values of two and three. There are several potential causes for this. First, the CDO interest values have a maximum of three during the night and a maximum of four during the day as discussed in Section 3. Some of the accumulation at an interest

value of three can be explained by this. In the future, division of the new storms into day and night regimes will be done before plotting the scatterplots to examine what differences the time of day may create. Second, recall that the membership function for the CC algorithm (Figure 3.1d) scales the appropriate categories to interest values of either one-half or unity which, after the weight of two is applied, become either unity or two, respectively. The CTOP and the GCD original values are scaled by the membership functions (Figure 3.1b,c) to include the full range of interest values between zero and unity. Thirdly, each point on the graph may contain many, many point-pairs that are indistinguishable. In the future a better method to represent the number of points will be employed.

6.3. Analyses of Various Scatter Plots

6.3.1. AMSR-E SST

It is a well-know fact that new storms tend to form over warm water in the ocean. As is shown in Figure 6.1, the scatterplot of the Advanced Microwave Scanning Radiometer (AMSR-E) sea surface temperature (SST) versus new-storm CDO interest values shows that most new storms formed where SST is >26.0°C. The approximate normal distribution of SST has a mean of 29.5°C and a standard deviation of 1.7°C. This result is consistent with high SST values during the summer.

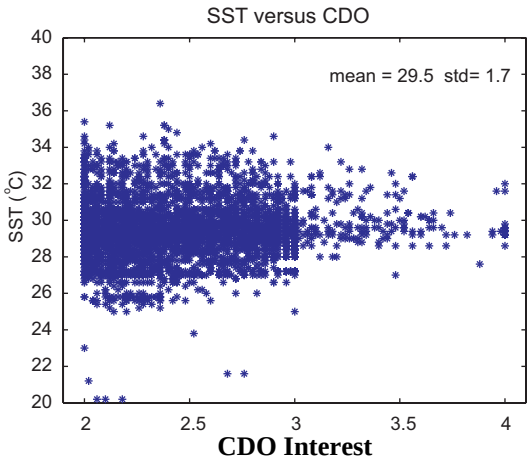

Figure 6.1. Scatter plot of AMSR-E SST versus CDO interest values associated with new storms for the Gulf of Mexico domain from Aug 12-23, 2007.

6.3.2. QUIKSCAT NEAR-SURFACE DIVERGENCE

Surface convergence associated with surface boundaries has long been recognized as a precursor of CI over the land. Over the ocean, surface-based CI studies have been lagging due to lack of observational data. Thanks to QuikSCAT near–surface wind measurements, the relation between surface convergence and CI over the ocean can be studied. A scatter plot of QuikSCAT-derived near-surface divergence versus CDO interest values of newly initiated storms is shown in Figure 6.2. New storms were associated with both near-surface convergence and divergence, with a slight bias toward convergence, as indicated by the mean divergence associated with all the new storms being -0.6×10^{-5} s^{-1}. The grid spacing used for the QuikSCAT wind field was 0.25 degrees in latitude/longitude,

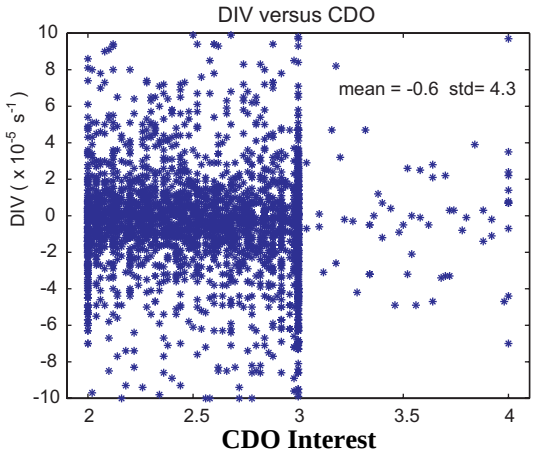

Figure 6.2. Scatter plot of QuikSCAT near-surface divergence versus CDO interest values associated with new storms for the Gulf of Mexico domain from Aug 12-23, 2007.

indicating that the smallest resolvable wavelengths are on the mesoscale rather than the convective scale.

6.3.3. AVERAGED RELATIVE HUMIDITY

Figure 6.3 shows a scatter plot of layer-averaged relative humidity above the top of boundary layer (between 875-625 mb) from the GFS model analysis versus the CDO interest values of new storms. New storm positions are matched to the horizontal projection of the layer-averaged relative humidity values. Clearly, new storms tend to form in an environment rich in moisture and rarely form when averaged relative humidity was less than 50%. The mean of all averaged relative humidity associated with CI is ~83%, with a standard deviation of ~10%.

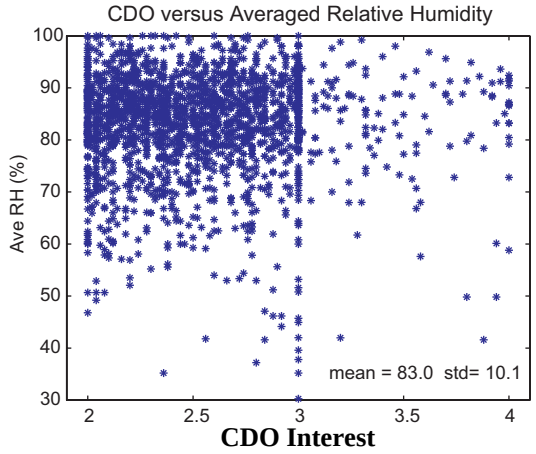

Figure 6.3. Scatter plot of averaged relative humidity versus CDO interest values associated with new storms for the Gulf of Mexico domain from Aug 12-23, 2007.

6.3.4. AIRS/AMSU AND GFS CAPE/CIN

Atmospheric Infrared Sounder (AIRS) and Advanced Microwave Sounding Unit (AMSU) provide vertical profile of atmospheric temperature and humidity that can be used to calculate standard convective parameters such as CAPE/CIN. The CAPE/CIN are calculated at 925 mb. For comparison, GFS surfaced-based CAPE and CIN fields are also obtained. The CAPE/CIN versus CDO interest scatter plots from both AIRS/AMSU and GFS are shown in Figure 6.4 and Figure 6.5, respectively. It is not surprising that both CAPE fields from AIRS/AMSU and GFS demonstrate no clustering in their distributions,

which is reinforced by the large standard deviation in Figure 6.4a,b. This result suggests that new storm formation can occur over a wide range of positive CAPE values. Considering the AIRS/AMSU CAPE is for air parcels at 925 mb while the GFS CAPE is surface-based, the mean value of CAPE from AIRS/AMSU and GFS are fairly similar.

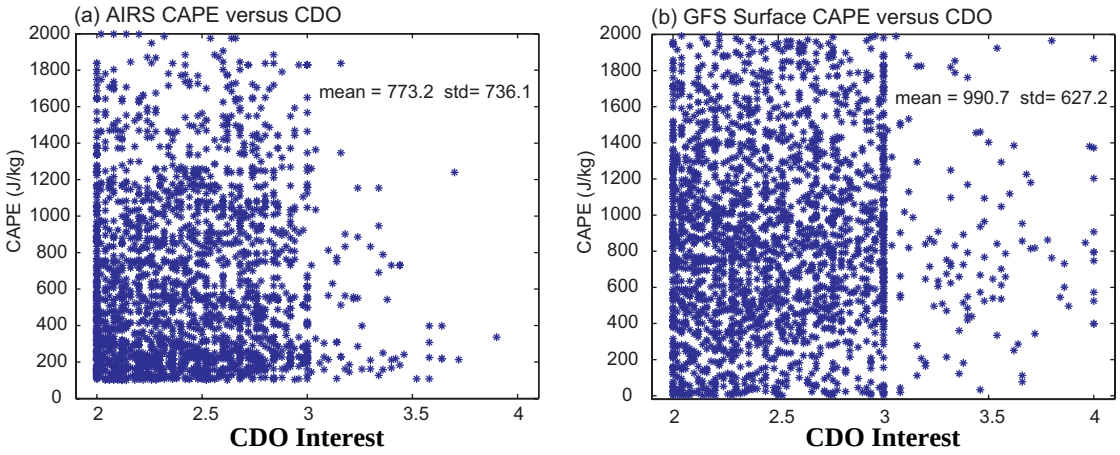

Figure 6.4. Scatter plot of a) AIRS/AMSU CAPE for 925 mb, and b) GFS surface CAPE versus CDO interest values associated with new storms for the Gulf of Mexico domain from Aug 12-23, 2007.

CIN fields from both AIRS/AMSU and GFS show clear trends that new storms tend to form in low/zero CIN regions, although high CIN values do not exclude CI. Convection initiation is the tug of war between two opposite forces, one is the upward forcing, and the other is the cap which needs to be penetrated before new storms can form. When convective forcing is strong, large CIN can still be destroyed.

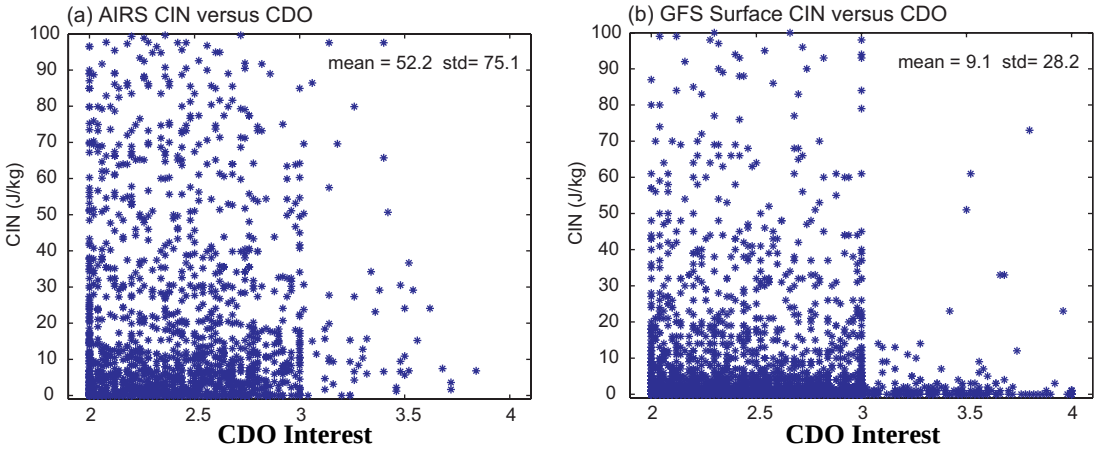

Figure 6.5. Scatter plot of a) AIRS/AMSU CIN for 925 mb, and b) GFS surface CIN versus CDO interest values associated with new storms for the Gulf of Mexico domain from Aug 12-23, 2007.

6.3.5. Frontal Likelihood Field

One method to find out if frontal forcing plays an important role in storm initiation is to look at the scatter plot of frontal likelihood field (Megenhardt et al. 2004; Kessinger et al.

2008) versus the CDO interest values of new storms. The frontal likelihood is an interest field derived from GFS model data such that high frontal likelihood interest values correspond to front locations. A scatter plot of frontal likelihood interests versus CDO of new storms is shown in Figure 6.6. No clear trend of frontal likelihood versus CDO is revealed, suggesting that frontal forcing may not be the sole important forcing mechanism in new storm formation over the Gulf of Mexico during August 2007. This result may vary during the year, in particular for the winter months.

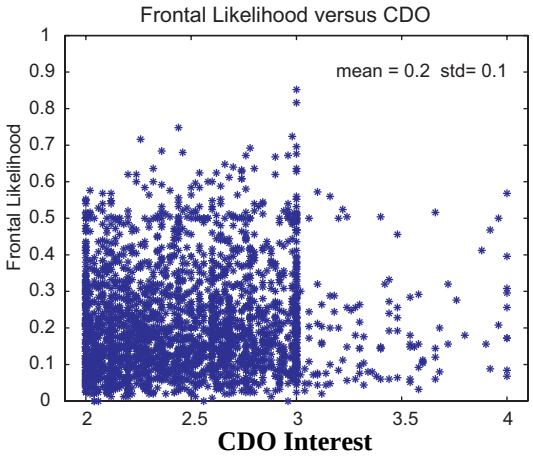

Figure 6.6. Scatter plot GFS-derived frontal likelihood interest field versus CDO interest values associated with new storms for the Gulf of Mexico domain from Aug 12-23, 2007.

6.4. Summary and Future work

In this preliminary study, a simple scatter plot approach is employed to study the relation between various environmental conditions and new storm formation over the Gulf of Mexico domain for a relatively short period in August 2007. Various satellite-based convective parameters were derived, which include 1) AMSR-E SST, 2) QuikSCAT divergence, 3) AIRS/AMSU CAPE/CIN, 4) GFS surface CAPE/CIN, and 5) GFS-derived averaged relative humidity and frontal likelihood field. It was found that SST, CIN and averaged relative humidity were potentially good discriminators of atmospheric conditions needed for convection initiation to occur, while CAPE and frontal likelihood field might not be good discriminators. However, many more analysis cases are needed to ascertain if these potential relationships hold true under all conditions and seasons.

7. Validation of the Current CNO system (NCAR)

With the goal of providing high resolution, tactical decision aids to oceanic pilots and dispatchers, short-term nowcasts of the location of convection, as identified by the CDO binary product, are produced for 1-hr and 2-hr intervals and displayed on the project web page (http://www.rap.ucar.edu/projects/ocn). The extrapolation is accomplished via a cell-tracking technique, called TITAN (Dixon and Wiener, 1996), also discussed in the previous section. The TITAN was developed for tracking 2- or 3-dimensional storms as identified by radar reflectivity, but for our purposes, the software performs similarly when used to track the 2-dimensional, binary CDO product. Instead of using a typical storm reflectivity value as the storm threshold, the threshold is reduced to 2.5 interest as discussed in Section 4.1. The TITAN extrapolates the storm cell position and anticipates

its growth and dissipation from past trends. A minimum storm size of 300 km^2 is a criterion that must be met before a storm is identified and then tracked.

For validation, a statistical comparison is done between the area enclosed by the TITAN shape at the forecast time and the CDO product ($\geq$2.5 interest) at the verification time for all forecasts produced between 12-22 August 2007, the period of Hurricane Dean's passage through the greater Gulf of Mexico region (see Section 2). Standard statistical indicators are computed with results shown in Table 7.1 for the Critical Success Index (CSI; Donaldson et al. 1975) and the bias (Wilks 1995). While this analysis does not provide a fully independent comparison such as is possible for the TRMM-CDO validation (see Section 4), this process does validate the extrapolation of CDO positions and is consistent with methodologies used for validating forecast skill over the CONUS (Pinto et al. 2006). The TRMM validation provides an estimate of the quality of the CDO binary product while this analysis provides an estimate of the quality of the CNO extrapolation process.

As expected, the best CSI performance is realized at the 1-hr nowcast (0.50) with declining performance at 2-hr (0.39) and 3-hr (0.31). Bias scores show a modest decrease with time from 0.79 to 0.76 to 0.74. The CNO CSI and bias scores produced for these 11 days compare favorably to those produced by the National Convective Weather Forecast - 6hr (NCWF-6) system (Pinto et al. 2006) for one day. The NCWF-6 is primarily a radar-based nowcasting system developed with FAA AWRP support to extend convective nowcasts to 6-hr using a blended observation- and NWP-based methodology. In the NCWF-6 analysis (Pinto et al. 2006), the CSI scores are plotted hourly over the diurnal cycle for a Great Plains squall line initiation case to illustrate performance differences related to convection initiation, extrapolation and dissipation. CSI scores for the 1-hr nowcast varied over the diurnal cycle from 0.2-0.4 and from 0.05-0.35 for the 2-hr nowcast with maximum scores realized several hours after the squall line formed. Further evaluation in the same vein is planned for the CNO.

Table 7.1. Statistical indicators are summarized for 1-hr, 2-hr and 3-hr intervals for the CNO for the period from 12-22 August 2007.

		Nowcast Period		
		1-hr	2-hr	3-hr
Indicators	Critical Success Index	0.50	0.39	0.31
	Bias	0.79	0.76	0.74
	Number of Forecasts	319	315	389

Figure 7.1 compares a 1-hr and 2-hr CNO nowcasts to the CDO binary product, both having the same verification time of 2315 UTC. The 1-hr nowcasts (cyan polygons in Figure 7.1a) enclose the CDO validation product fairly well. The polygons tend to be

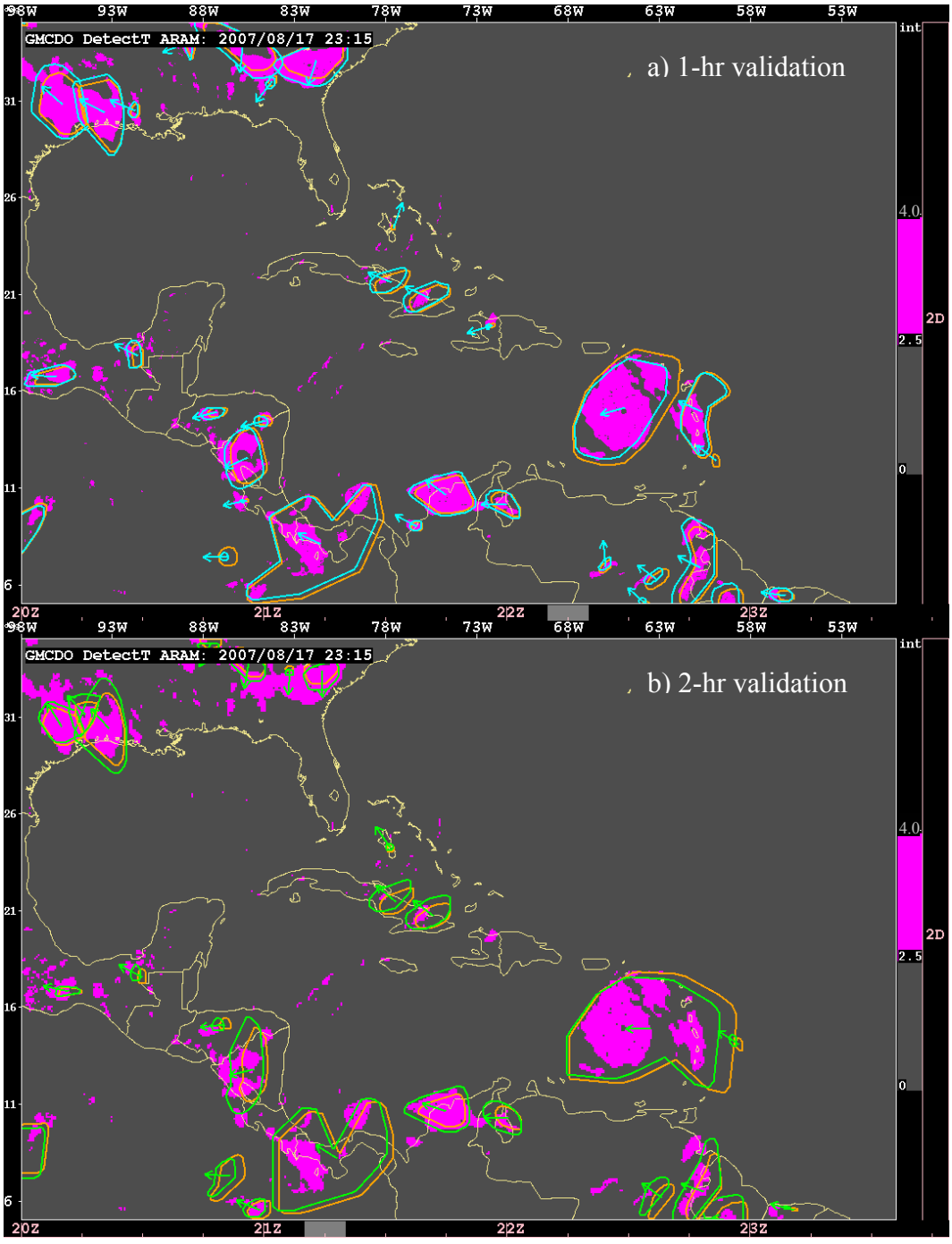

Figure 7.1. For 17 August 2007, the CDO (magenta shapes) is shown at the validation time of 2315 UTC for the a) 1-hr nowcast made at 2215 UTC and for the b) 2-hr nowcast made at 2115 UTC. The position of the CDO at the respective forecast times is indicated in both panels by orange polygons. The 1-hr CDO nowcast is indicated in a) with the cyan polygons and the 2-hr nowcast is in b) with green polygons. Vectors (arrows) indicate storm motion but are not proportional to storm speed.

generous in size compared to the area of the CDO with occasional location displacements. In Figure 7.1b, the 2-hr nowcast polygons show similar results with some reduction in performance. For both, the position predictions for Hurricane Dean validated very well.

8. Nowcasting using Random Forest Classification (NCAR)

8.1. Introduction

The traditional methodology employed within nowcasting systems involves an extrapolation scheme that either tracks storms as objects or looks for correlations between time periods to ascertain a storm motion vector. The CNO, which utilizes an object-tracker called TITAN (Dixon and Weiner, 1993) as its extrapolation scheme, is one such example. The novel method of using random forest classification for nowcasting takes a completely different approach. In machine learning, a random forest is a classifier that consists of many decision trees and outputs the class that is the mode of the class voted by each individual tree. As a promising technique, random forest has been widely applied in various scientific fields, including the development of the FAA's Consolidated Storm Prediction for Aviation (CoSPA).

The wide usage of random forest is the result of a number of advantages this technique can provide as a statistical classifier. Some of the prominent advantages are listed below.

1) Handles a very large number of input variables and produces a highly accurate classifier;
2) Estimates the importance of input variables in determining classification. The relative importance of each input variable can be used to select the most effective predictors for classification;
3) Handles missing data relatively well;
4) Training the forest is fast;
5) Provides an experimental way to detect variable interactions;
6) Computes proximities between cases, which is useful for clustering, detecting outliers, and visualization of data by scaling.

The following sections will describe the procedures of running random forest and present some preliminary results of nowcasting oceanic convection using the random forest classification.

8.2. Procedures of training the random forest and classifying using the trained forest

A set of predictors derived from geostationary and polar-orbiting satellites and the GFS numerical model are used as input variables to the random forest. The output variable (i.e., the forecast), which represents oceanic convection, is the CDO interest field. The goal of nowcasting oceanic convection is thus converted to forecasting CDO intensity, which ranges in values between 0 and 4, by using a set of predictors derived from satellite observations and GFS model fields.

The flow chart of training and subsequent classification using the trained forest is shown in Figure 8.1. As a first attempt of exploring the random forest technique in oceanic weather, seven days of data (12-18 August 2007 from Hurricane Dean; see Section 2) are used to train a forest of 200 decision trees, while data from another four days (19-22 August 2007 also from Hurricane Dean) are used for independent classification and

verification. An initial set of 17 predictors, which includes various satellite and GFS model-derived fields over the Gulf of Mexico domain, is employed in the random forest training/classification. All the satellite-based input predictors are advected 1-2 hr into the future using motion vectors derived by blending TITAN vectors with GFS steering level winds. Both the input predictor fields and the validation CDO interest field are converted from MDV (Meteorological Data Volume, an internal NCAR format) to ARFF (Attribute-Relation File Format) format, a format the random forest software can read. The ARFF files are then thinned and used for training a forest with 200 decision trees. To achieve reasonable accuracy, at least 100 decision trees are needed. The trained forest is used for independent classification/verification for four other days.

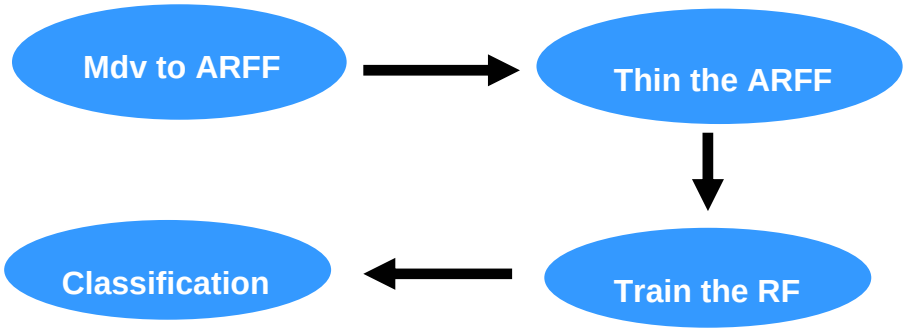

Figure 8.1. Flow chart for training the random forest and for classifying using the trained forest.

The random forest produces votes of each CDO interest category (i.e., CDO interest value equals 0, 1, 2, 3 or 4) for each set of input predictors at forecast time. When it was found that the classification process, which creates the 1-hr forecast, could take ~1hr to run, we decided to thin the ARFF input file by using cloud top height as a threshold. Only regions with cloud top height over 10,000 ft are classified. By reducing the number of input grid points, the classification process takes ~20 min to run. Certainly the reduction in computing time depends on the weather condition inside the domain.

One example of the votes for CDO interest equals 0, 1, 2, 3 and 4 is shown in Figure 8.2. Hurricane Dean can be seen clearly in the middle of the domain. As you would expect, the majority of the domain with no convection has most decision trees voting CDO = 0 (see Figure 8.2a); at the same time, very few decision trees vote yes in the convection-free region for CDO values greater than zero. The strong convection associated with Hurricane Dean has the majority of trees voting CDO interest = 3 (see Figure 8.2d).

An example of a 1-hr random forest forecast of CDO and its corresponding verification is shown in Figure 8.3. It is interesting to notice that a CDO interest forecast purely derived through decision tree votes looks very similar to the CDO validation field, considering totally different techniques are used in calculating them. The random forest forecast was able to capture Hurricane Dean as well as other relatively weak convection over the Gulf of Mexico. It should be pointed out that the random forest forecast seemed unable to

(a) Votes for CDO = 0

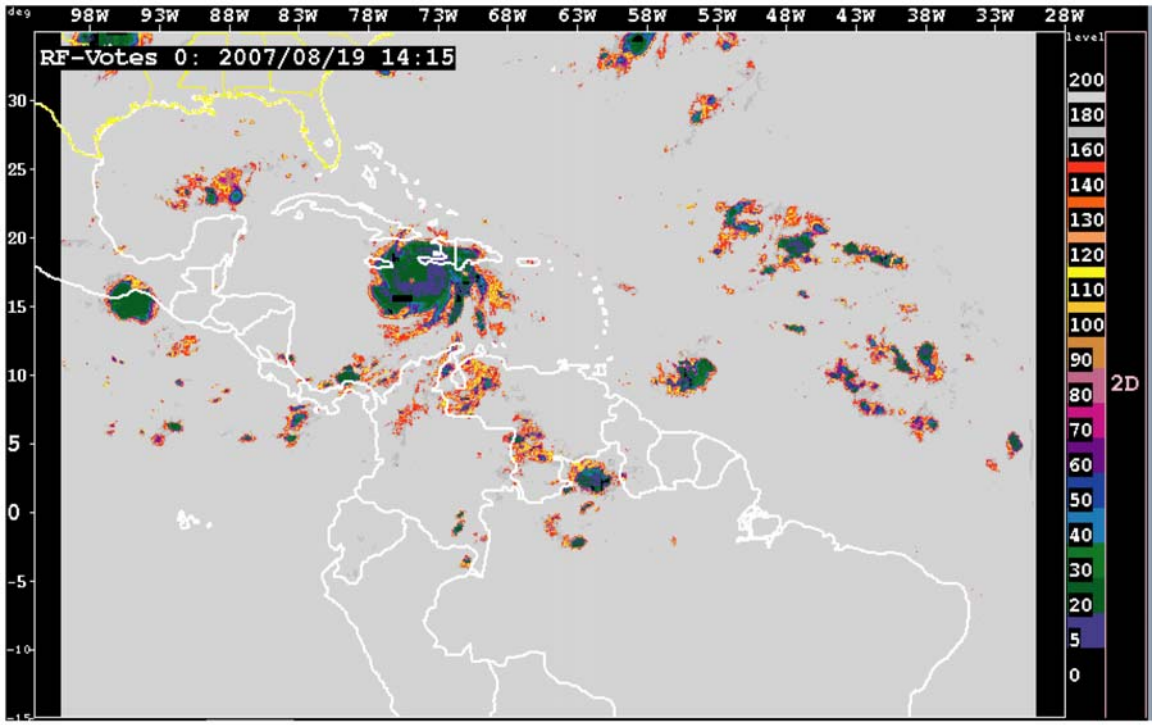

(b) Votes for CDO = 1

Figure 8.2. An example showing the number of votes the random forest produced for various CDO interest values at 1415 UTC on August 19, 2007 over the Gulf of Mexico domain for a) CDO interest = 0 and b) CDO interest = 1. Figure continued on next page.

(c) Votes for CDO = 2

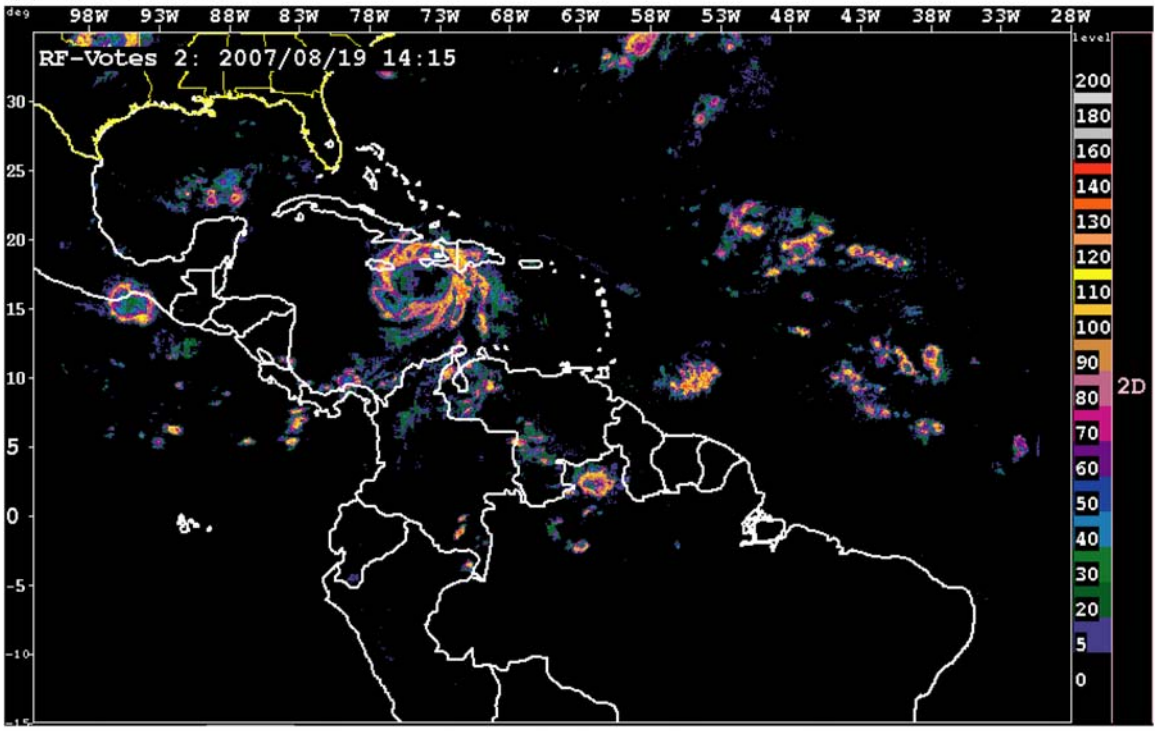

(d) Votes for CDO = 3

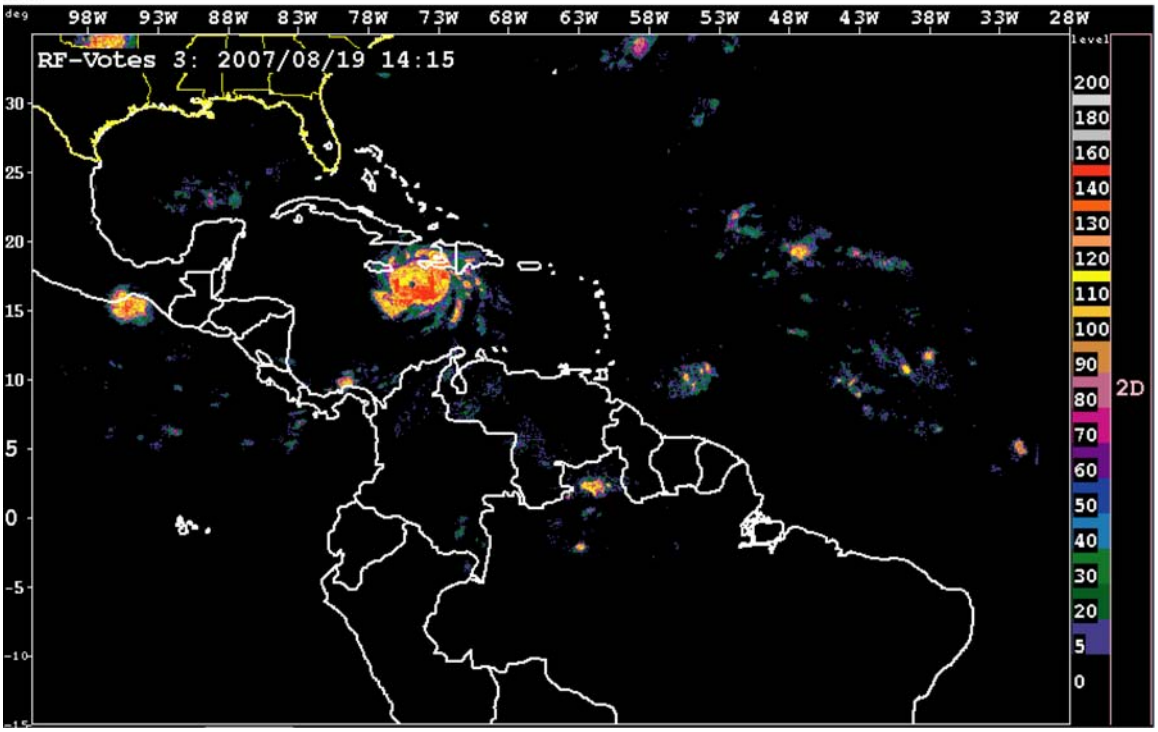

Figure 8.2, con't. An example showing the number of votes the random forest produced for various CDO interest values at 1415 UTC on August 19, 2007 over the Gulf of Mexico domain for c) CDO interest =2 and d) CDO interest = 3. Figure continued next page.

(e) Votes for CDO = 4

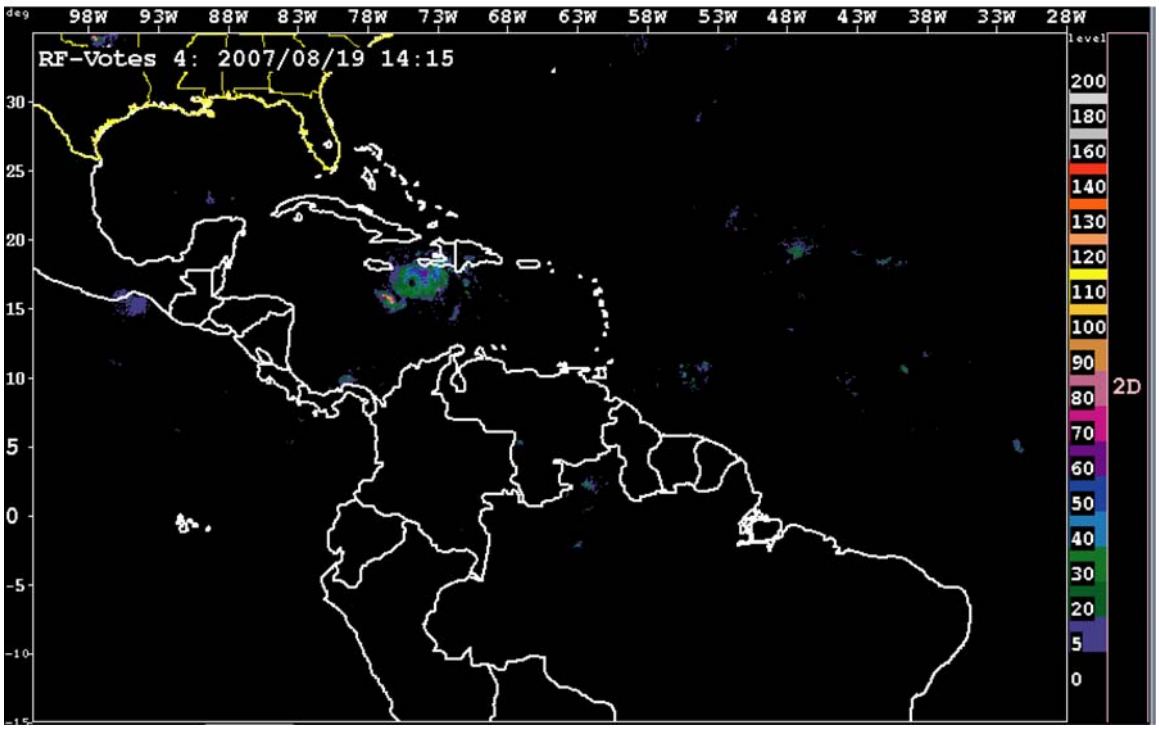

Figure 8.2, con't. An example showing the number of votes the random forest produced for d) CDO interest = 4.

forecast CDO = 4 very well, therefore, some calibration might be needed for better verification results.

8.3. Future Work

While this first attempt to use the random forest machine learning technique to nowcast oceanic convection has shown promise, plenty of improvements can be pursued in the near future. First, the input predictor list will be expanded to include more fields; secondly, the forecast should be extended to 2-hrs; and finally, statistical verification should be performed on the CDO interest forecast from random forest so that its performance can be compared to the current CNO performance.

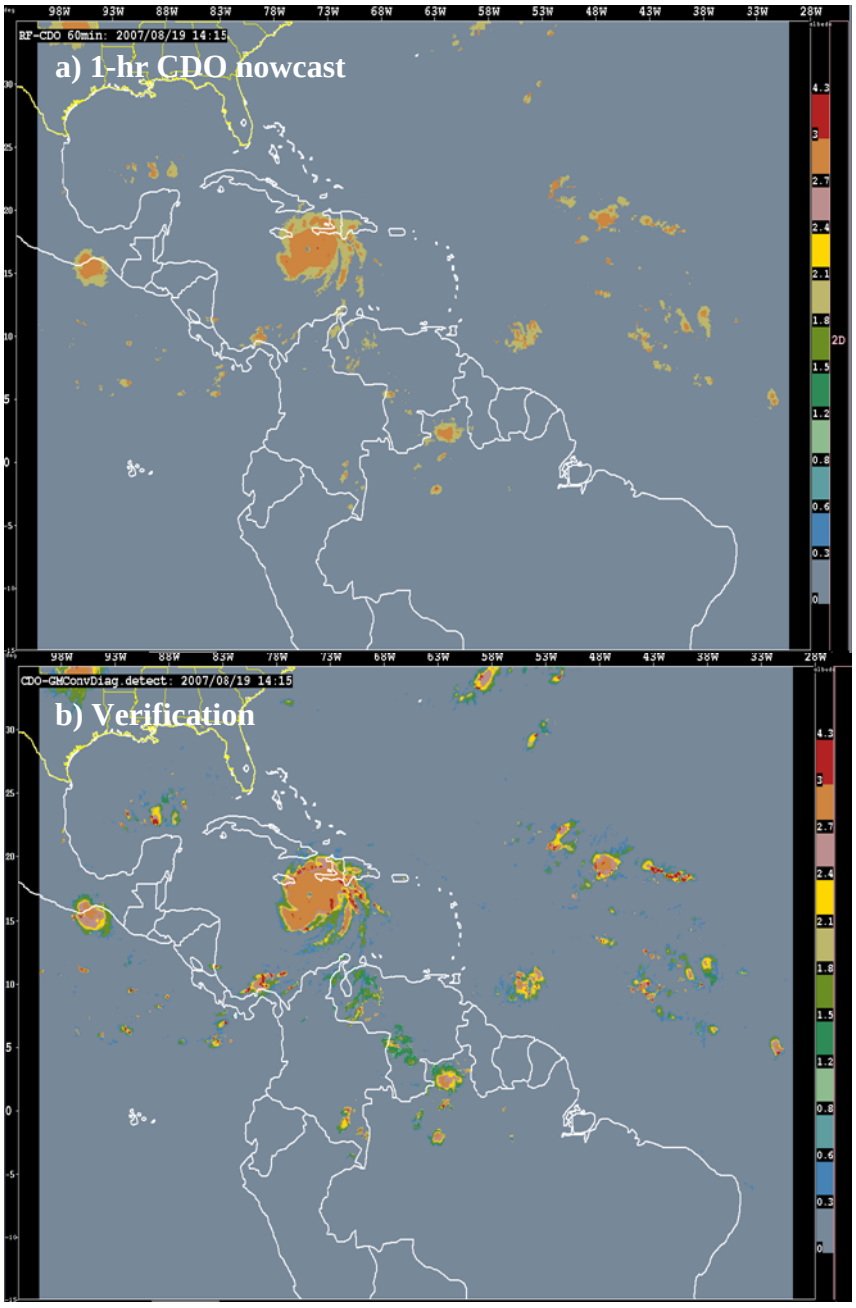

Figure 8.3. An example of random forest created CDO 1-hr forecast and its corresponding verification at 1415 UTC on August 19, 2007 over the Gulf of Mexico domain. a) 1-hr CDO random forest forecast, and b) CDO verification.

9. Use of Geostationary-Tracked Winds for Storm Extrapolation (NCAR)

Within the CNO system, the TITAN object tracker provides the initial estimates of storm motion for cells identified by the CDO product. However, this initial wind field is frequently noisy due to fluctuations in storm position upon which TITAN depends. Within the CNO system as currently configured, the initial TITAN storm motion vectors are merged with the GFS gridded winds at 700 mb to improve performance of the storm

extrapolation. The winds at 700 mb are assumed to be the steering winds for deep convection. Once the merger is accomplished, spatial and temporal filters are applied to produce the final extrapolation wind field that is used to nowcast storm position. The GFS model has relatively coarse resolution with a grid spacing of 0.5 degrees in latitude and longitude.

Cloud motion vectors (CMV) have been derived from geostationary satellite imagery (Visible, infrared and water vapor channels) for many years (Menzel 2001) and are available operationally from the National Oceanic and Atmospheric Administration (NOAA) at approximately 3-hr intervals. The NRL also has CMVs available and they are providing these data for this effort.

During the data assimilation processing for the GFS, the CMV are input as a data source. However, these winds frequently reflect mesoscale motions that the global model must necessarily reject since the motion scales are at too fine a scale. Therefore, merging CMV with the GFS winds can, theoretically, return mesoscale motions that may be important for determining the correct trajectory for a storm. To test this possibility, an effort is underway to measure extrapolation performance using varying wind fields from either TITAN merged with GFS winds or TITAN merged with GFS and CMV to see what effect the CMV may have on storm motion prediction.

A preliminary example (Figure 9.1) shows that the CDO with the TITAN 2-hr nowcasts of storm position indicated by the polygons. The TITAN storm motion vector is also indicated along with the storm speed, and the CMV between 750-650 mb are also plotted. To better compare the CMV to the TITAN storm motion vectors, the left portion of Figure 9.1 is magnified and displayed in Figure 9.2. As Figure 9.2 shows, the CMV and the TITAN storm motion vectors frequently agree in direction, if not speed. However, there are also some notable exceptions where the two vectors do not agree. This work is in preliminary stages and the reason for the disagreement between the two is not known as of this writing but will be investigated.

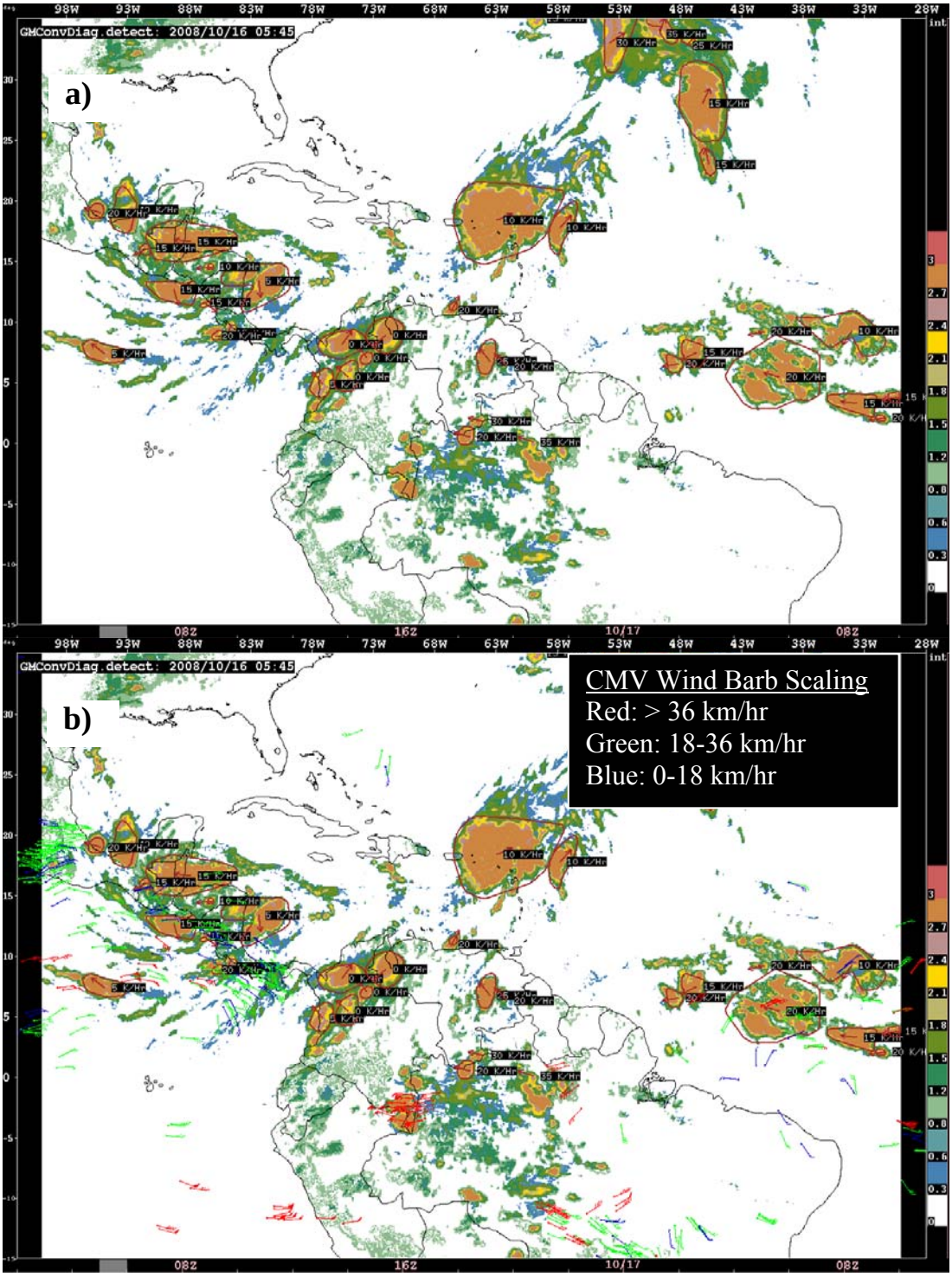

Figure 9.1. In both a) and b) the unthresholded CDO interest field is shown from 16 October 2008 at 05:45 UTC with the TITAN polygons (brown polygons) that indicates the 2-hr nowcast of storm position along with the storm motion vector (not proportional to storm speed) and storm speed (text). In b) the CMV between 750-650 mb, up to 3-hr prior are plotted following the key in the upper right. Wind speeds are plotted in km/hr with a full barb equal to 10 km/hr.

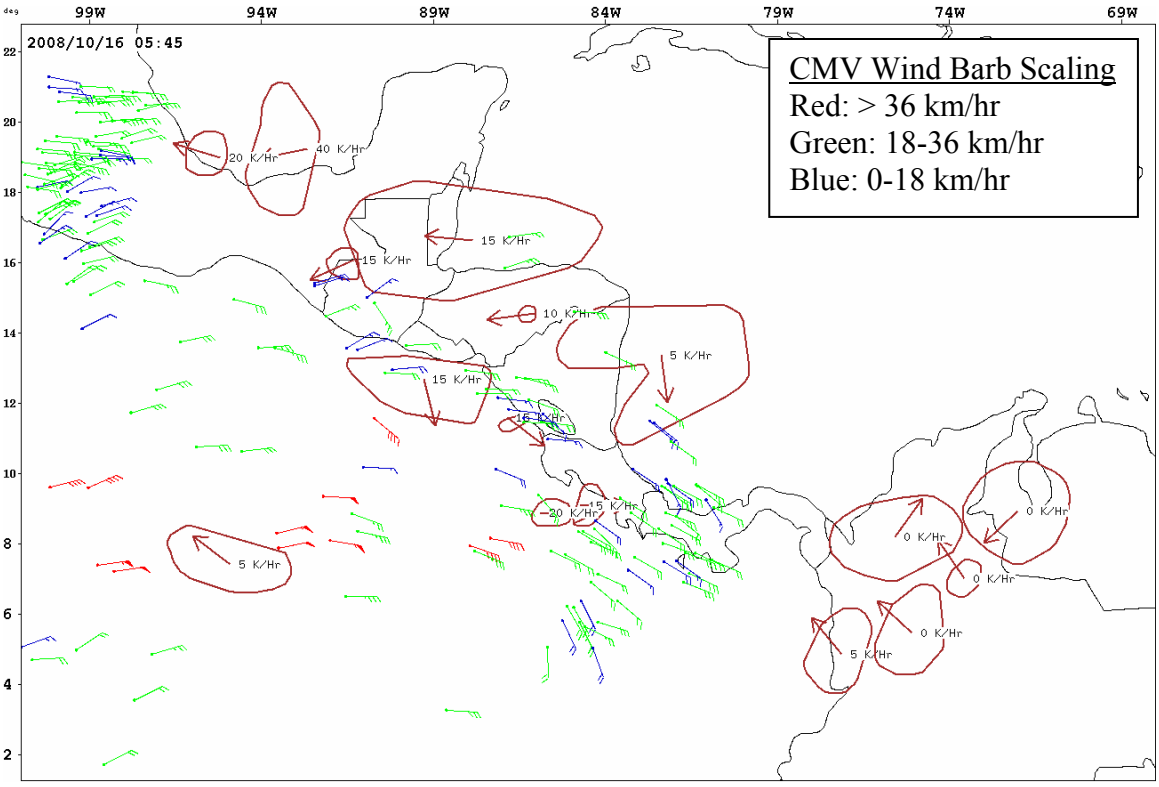

Figure 9.2. A comparison is shown of the CMV and the TITAN storm motion vectors (not proportional to storm speed) and storm speed (text). The domain is a subset of that shown in Figure 9.1 (left quadrant).

10. Comparison of African Dust and Lightning Activity in the Area of Miami, Florida and the Gulf of Mexico (MIT LL)

To examine the possibility that observations of dust transport from Africa could assist in efforts to nowcast the level of convection/lightning activity in the greater Gulf of Mexico region, a brief feasibility study was conducted by Earle Williams, MIT LL, in collaboration with J. M. Prospero, University of Miami, and V. Phillips, University of Hawaii with results presented here. Dr. Williams was funded by this ROSES grant while Drs. Prospero and Phillips were funded by their universities. The goal of this study was to ascertain if the inclusion of aerosol observations from the Cloud-Aerosol Lidar and Infrared Pathfinder Satellite Observation (CALIPSO), as an additional indicator into the CNO system for the Random Forest technique, would produce positive impacts on nowcast performance.

10.1. Introduction

The interest in aerosols that modulate cloud microphysics, and thereby cloud dynamics, precipitation and lightning, has increased in recent years (Rosenfeld et al., 1999; Orville et al., 2001; Williams et al., 2002; Steiger and Orville., 2002) The basic idea is that when an updraft is polluted with aerosol (with cloud condensation nuclei), the available liquid condensate is shared among a larger number of nucleation sites, so the cloud droplets are smaller than they otherwise would have been in cleaner conditions. The immediate impact is that the coalescence of cloud droplets is suppressed, and consequently

precipitation as well. A secondary impact is that the available cloud water can rise higher in the cloud and into the mixed phase region where it can participate in the Bergeron process and the riming growth of graupel, and thereby invigorate the process of cloud electrification and lightning (Williams et al, 2002). There is particular interest in these ideas in the tropical maritime environment (such as the Gulf of Mexico considered here) which is ordinarily aerosol-sparse and whose main mechanism for precipitation formation is the warm rain process at sub-freezing temperatures, and where lightning is ordinarily scarce. This is the context of recent interest in a role for aerosol in the invigoration of hurricanes (Rosenfeld et al., 2007), and the lightning activity within them (Jenkins et al., 2008).

Field tests for a role for aerosol (and thermodynamics) in lightning activity have been previously carried out in Brazil (Williams et al, 2002) during the NASA TRMM LBA campaign in 1999-2000. Though intense lightning activity was observed during the polluted pre-monsoon regime there, it was also observed during the clean phase that followed. The overall conclusion was that the aerosol played only a secondary role (to thermodynamics) in influencing the electrical activity in the rainforest region of Rondonia under study there.

A positive anomaly in lightning activity over heavily polluted Houston, Texas has been documented (Orville et al., 2001; Steiger and Orville, 2002) with the National Lightning Detection Network—roughly an enhancement of a factor-of-two relative to adjacent areas. One explanation for the positive anomaly has been the existence of urban aerosol exacerbated by the oil refineries there. An alternative explanation is the urban heat island effect that serves to invigorate convective activity by providing greater instability. Support for the latter interpretation and against a role for aerosol is the evidence that precipitation in the Houston areas is enhanced, not suppressed (Shepherd and Burien, 2003).

The prodigious African dust source provides additional opportunities to study the impact of dust on convective vigor and lightning. Africa is the largest source of mineral aerosol in the world. In prevailing easterly flow in northern hemisphere (NH) summer months, large quantities of dust are swept off Africa and advected to the Americas. The Saharan Air Layer (SAL) is one mode of synoptic scale dust transport, and is accompanied by a temperature inversion that also translates all the way to the Americas. Dr. Joseph Prospero has maintained dust monitoring sites in Barbados (Prospero and Lamb, 2003) and in Miami, Florida (Prospero et al., 1987) that are close to the Gulf of Mexico region that is of interest for the Oceanic Convective Diagnosis and Nowcasting work.

An initial look at the impact of African dust on cirrus cloud was possible during the Crystal Face experiment in Florida (Sassen et al., 2003). As a follow-on to this experiment, Van den Heever et al. (2006) conducted a modeling study that incorporated aerosol effects. Greater updrafts were documented in the models when aerosol was prevalent.

This study is concerned with the observational tests of the role of African dust on lightning activity in the vicinity of the dust-measuring site in Miami. Two possible modes of behavior were anticipated on the basis of foregoing ideas and experience: (1) the lightning activity would be enhanced by the presence of dust and (2) the entire population

of moist convection (and attendant lightning) is suppressed by the occurrence of the inversion accompanying the SAL. This study is concerned with an examination of these questions with coordinated observations of dust and lightning.

10.2. Methodology

The observation of dust loading in the atmosphere in Miami, Florida (25.75 N, 80.25E) has been described by Prospero et al. (1987). On the basis of filter capture of mineral aerosol extracted from fixed volumes of air, the daily mean dust loading in micrograms per cubic meter is derived. These observations are available for the period 1989-2006.

The continuous observation of cloud-to-ground lightning activity (in both negative and positive polarity) is available over the continental US by the National Lightning Detection Network (NLDN; Cummins et al., 1998). The location accuracy in many locations of the US, including the Florida area, is now better than 1 km. For purposes of comparison with the measured dust, daily lightning totals (of both polarities, and by the UT clock) were computed within two circular areas of 250 km radius, one centered on the dust collection site in Miami, Florida (25.75^{o} N, 80.25^{o} E) and one centered on a location in the Gulf of Mexico (26^{o} N, 85^{o} W) where the Lincoln Laboratory TRMM satellite validation effort is underway with NCAR.

10.3. Preliminary Results

The initial time series of dust was taken from 1996 and prepared for this study by J. Prospero, on the basis that this year was a very methodical one for data collection. The four panels of Figure 10.1 show the simultaneous time series for dust and for lightning for each of two circular domains, and for negative and positive lightning flashes. The days with the largest dust loading are July 25-26, 1996 and were also days with no detected lightning. Further investigation of satellite imagery for this day showed an absence of moist convection over the entire region of south Florida and the Gulf of Mexico, supporting the idea that the inversion associated with the dust intrusion was also inhibiting the convection. Other episodes in the record (July 4-5, 1996; August 7-8, 1996) suggested that the dust might be invigorating the lightning.

Additional time series were explored in 1997 for the Miami area. These plots are shown in Figure 10.2. Again, pronounced lightning days are noted with and without accompanying dust enhancements. During some periods of greatly enhanced dust (July 17-20, 1997; August 3-5, 1997), the lightning drops again to near zero. Additional time series comparisons for 1998 are shown in Figure 10.3.

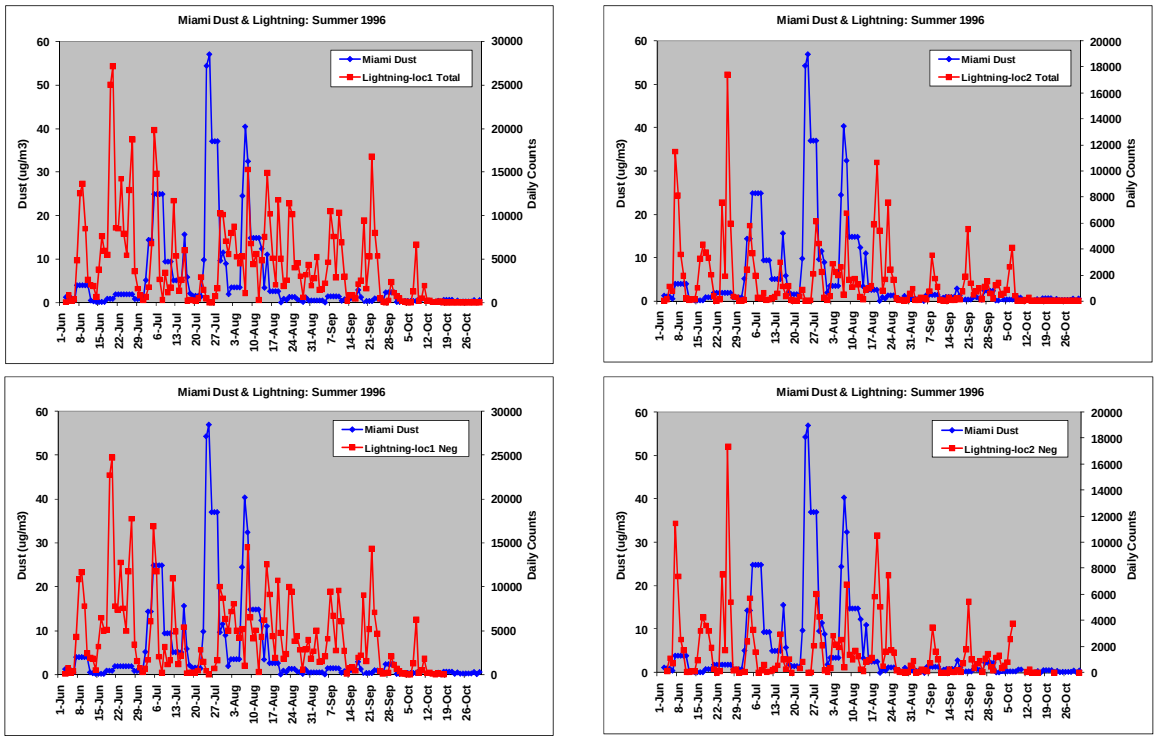

Figure 10.1. Initial time series of dust and lightning for two circular regions defined in the text, and for both negative and positive lightning polarities, for 1996.

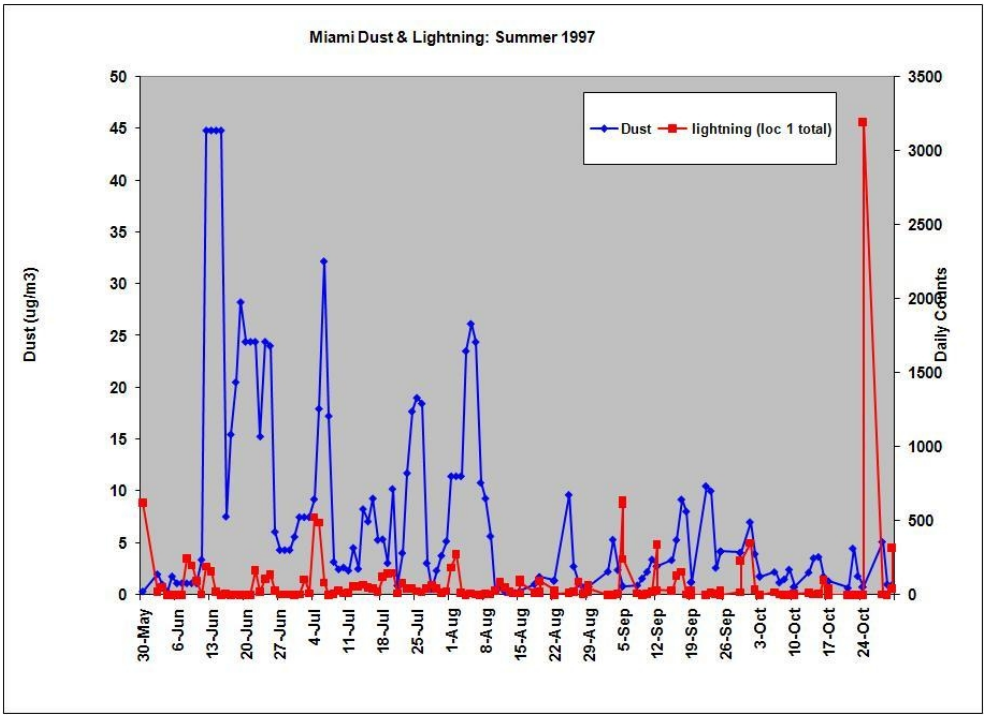

Figure 10.2. Time series comparisons of daily dust and lightning for the Miami area in 1997.

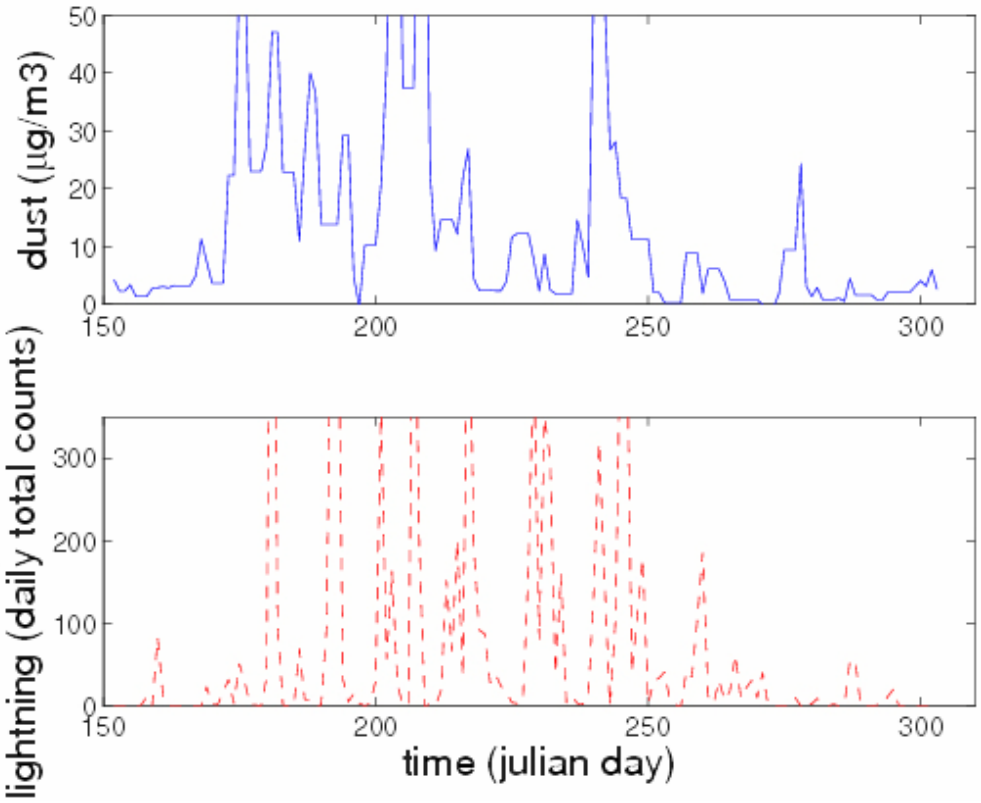

Figure 10.3. Time series comparison of dust (top) and daily total cloud-to-ground lightning flashes (bottom) for the Miami area in 1998.

A correlation plot of daily dust loading and daily lightning totals is shown in Figure 10.4. Little positive correlation is apparent, when all the days with lightning and dust are considered. The correlation coefficient of the least squares fit is only 0.28.

An additional test was undertaken to compare the distribution of dust loading on days with and without any lightning. The results are shown in histogram form in Figure 10.5. Despite the occurrence of the complete shutdown of lightning on the most heavily dust-laden day in 1996 and on other days in 1997, here one does not see a tendency for days without lightning to have systematically large dust loadings (suggestive perhaps of stronger temperature inversions). One does see however a tendency for greater amounts of dust on days with lightning, than on days without.

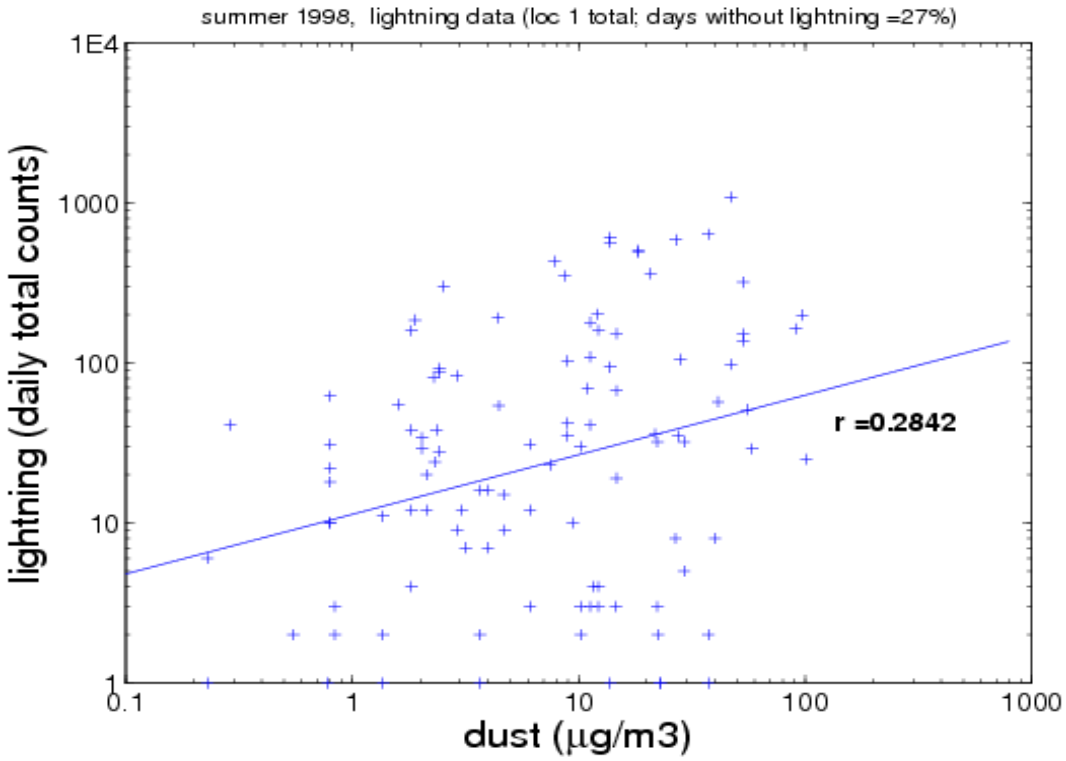

Figure 10.4. Correlation plot of daily dust loading versus daily lightning totals for observations in the Miami area for 1998. The correlation coefficient of the least squares fit is 0.28.

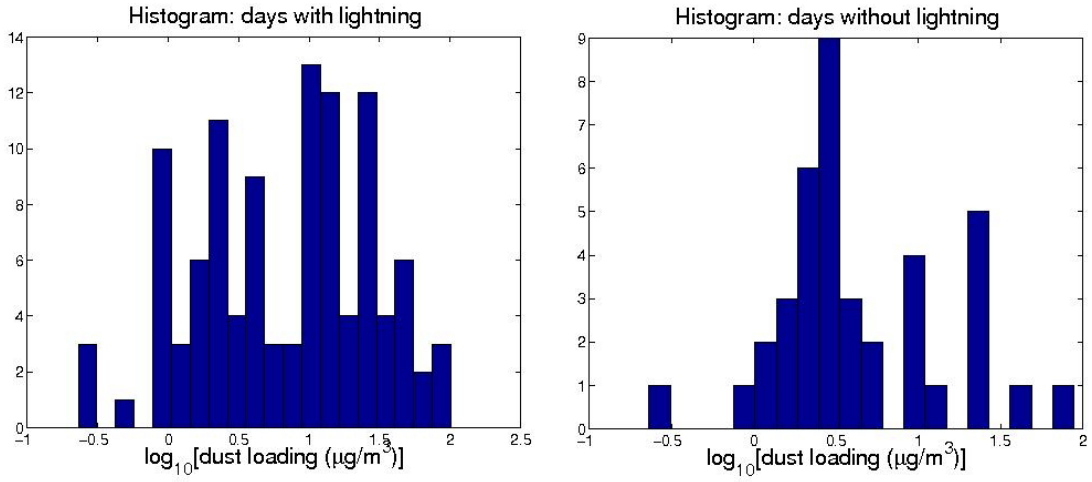

Figure 10.5. Histograms of numbers of days with specific dust loadings, for all days with lightning (left) and days without lightning (right) for observations in the Miami area in 1998.

10.4. Discussion and Conclusion

The absence of a tightly correlated behavior between daily dust content and daily lightning activity casts doubt on a primary role of the dust in influencing the convective intensity and lightning activity of the storms under investigation. This finding is broadly consistent with conclusions reached in Williams et al (2002) for the role of aerosol (produced by biomass burning) on lightning activity. In light of earlier findings supporting a primary role for thermodynamics in the lightning activity, it would be valuable to confirm such a tendency in the observations at hand by investigating measures of thermodynamically-controlled instability over the same time period. If satellite or radar measures of the individual storm cells contributing to the integrated lightning activity were available, it would also be valuable to implement some normalization for the number of lightning flashes per storm to correlate with the estimates for dust loading.

Due to the lack of correlation between aerosol content and lightning activity, use of CALIPSO data within the CNO system will not be pursued. Further, the CALIPSO provides only vertical cross-sections through hazardous convection in contrast with the three dimensional information available with the TRMM radar data. Vertical cross-sections provide for poor samples of convective cloud height, for example. The CALIPSO data are better suited for looking at long, two dimensional features, like the Intertropical Discontinuity (ITD) in Africa or the Pacific Intertropical Convergence Zone (ITCZ), as possible examples.

General Topics

11. Enhancements to the Web Site (NCAR)

The project web site has added a new domain for display of cloud top height product over the North Atlantic (Figure 11.1). This region was added at the request of an international dispatcher from Continental Airlines working out of Houston, TX, who has found the entire project web site quite useful. The display updates as soon as imagery is available.

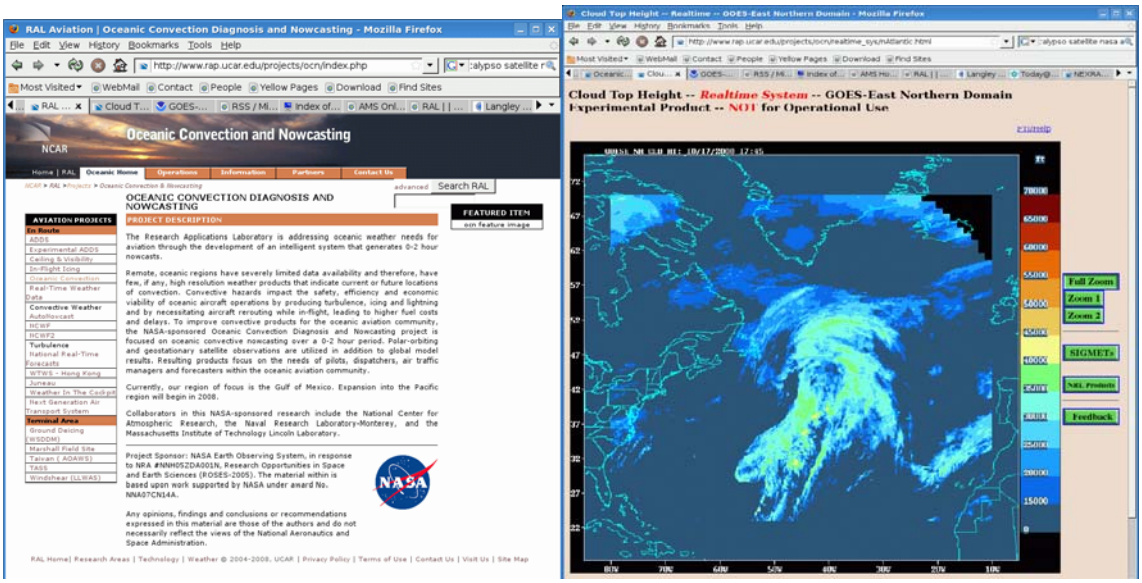

Figure 11.1 Project web pages are shown (http://www.rap.ucar.edu/projects/ocn) by the (left) main page and (right) the cloud top height product shown over the new North Atlantic domain.

For Year 3, the new Pacific domain will be added to the Product Suite on the web site.

12. Summary of Year 2 and Outlook for Year 3 (All Labs)

Considerable progress has been achieved during Year 2 of this proposal and is particularly notable given the long delay in securing the contractual agreement between NCAR and MIT LL. Validation of the CDO product using TRMM products showed that it has skill at detecting convection and that the threshold of 2.5 provides the best performance. Preliminary efforts to utilize the Random Forest machine learning technique to improve upon current techniques within the CNO shows promise and will continue to be investigated. The current methodology within the CNO (i.e., using TITAN for storm tracking) was validated and found to have skill for 1-hr and 2-hr nowcasts. Investigation into atmospheric and oceanic characteristics in the presence of convection initiation was accomplished to further our understanding of oceanic convection. The NRL GOES Cloud Classifier algorithm updates were successful and ensure that the algorithm can eventually be utilized within the NWS and/or the AWC. Initial testing of the Cloud Classifier has been accomplished for the MTSAT satellite and will be completed during Year 3, enabling the project expansion into the Pacific Ocean domain. A comparison of the Cloud Classifier to the cloud typing algorithm of Pavolonis

and Heidinger (adapted for use at NRL by S. Miller and C. Mitrescu) showed that the algorithms, for the most part, produce comparable results, thus strengthening the confidence in the classifier output. A study was completed to examine the possibility of using African dust transport into the Gulf of Mexico region as an indicator for convective suppression or enhancement but results were counter to their use within the CNO. Ingesting Cloud Motion Vectors into the operational system has been accomplished; further work is required to investigate and validate their usefulness in storm extrapolation. The addition of the North Atlantic domain into the web display of the cloud top height product was completed.

During Year 3 of this project, expansion of the CDO/CNO capability into the Pacific domain will be accomplished over a yet-to-be determined domain. Completion of studies that were begun during Year 2, such as the Random Forest and the use of cloud motion vectors, will be completed and implemented if found to be an improvement over existing techniques. Methodology to evaluate the CDO using TRMM will be adapted to validate the CNO 1-hr and 2-hr nowcasts.

13. Papers Submitted (All Labs)

One journal article appeared in the January 2008 issue of the *Journal of Applied Meteorology and Climatology*, as follows:

Donovan, M.F., E.R. Williams, C. Kessinger, G. Blackburn, P.H. Herzegh, R.L. Bankert, S. Miller, and F.R. Mosher, 2008: The identification and verification of hazardous convective cells over oceans using visible and infrared satellite observations. J. Appl. Meteor. and Clim., 47 (1), 164-184.

One reviewed paper was submitted and presented at the SPIE Conference in San Diego during August 2008. The paper was published in the SPIE Proceedings, as follows:

Kessinger, C., M. Donovan, R. Bankert, E. Williams, J. Hawkins, H. Cai, N. Rehak, D. Megenhardt, and M. Steiner, 2008: "Convection diagnosis and nowcasting for oceanic aviation applications" in Remote Sensing Applications for Aviation Weather Hazard Detection and Decision Support, edited by Wayne F. Feltz, John J. Murray, Proceedings of SPIE Vol. 7088 (SPIE, Bellingham, WA, 2008) 7088-08, San Diego, 10-14 August 2008.

Three papers were submitted and presented at the AMS Annual Meeting held in New Orleans during January 2008.

Bankert, R.L., C. Mitrescu, S.D. Miller and R.H. Wade, 2008: Comparison of GOES cloud classification algorithms employing explicit and implicit physics, *Proceedings, 5th GOES Users' Conf.*, Amer. Meteor. Soc., New Orleans, LA, 20-24 Jan 2008.

Cai, H., C. Kessinger, N. Rehak and D. Megenhardt, 2008: Investigation into environmental conditions for storm initiation over the ocean using satellite data. 13th Conf. on Aviation, Range, and Aerospace Meteorology, Amer. Meteor. Soc., New Orleans, LA, 20-24 Jan 2008.

Kessinger, C., H. Cai, N. Rehak, D. Megenhardt, J. Hawkins, and E. Williams, 2008: Oceanic Convection Diagnosis and Nowcasting. 13th Conference on Aviation,

Range, and Aerospace Meteorology, American Meteorology Society, New Orleans, LA, 20-24 January 2008.

The conference paper by Williams et al. (below) was not funded by this ROSES-2005 award, but is shown to indicate the leveraging that is occurring within NCAR/RAL to use the Random Forest technique for nowcasting. This paper was presented at the AMS *6th Conference on Artificial Intelligence and its Applications to the Environmental Sciences*.

Williams, J.K., D. Ahijevych, C. Kessinger, T. Saxen, M. Steiner, and S. Dettling, 2008: A machine learning approach to finding weather regimes and skillful predictor combinations for short-term storm forecasting. 6th Conference on Artificial Intelligence and its Applications to the Environmental Sciences, American Meteorology Society, New Orleans, LA, 20-24 January 2008.

Three abstracts were submitted to the *16th Conference on Satellite Meteorology and Oceanography* for the American Meteorological Society Annual Meeting to be held in Phoenix, AZ during 11-15 January 2009. They are:

Cai, H., C. Kessinger, D. Ahijevych, J. Williams, N. Rehak, D. Megenhardt, R. L. Bankert, J. Hawkins, M. F. Donovan, E. R. Williams, 2009: Nowcasting oceanic convection using Random Forest classification.

Donovan, M. F., E.R. Williams, C. Kessinger, N. Rehak, H. Cai, D. Megenhardt, R.L. Bankert, and J. Hawkins, 2009: An evaluation of a convection diagnosis algorithm over the Gulf of Mexico using NASA TRMM observations.

Kessinger, C., H. Cai, N. Rehak, D. Megenhardt, M. Steiner, J. Hawkins, R. Bankert, M. Donovan, and E. Williams, 2009: The oceanic convection diagnosis and nowcasting system.

14. References

Bankert, R.L. and R.H. Wade, 2007: Optimization of an instance-based GOES cloud classification algorithm, *J. Appl. Meteor. Clim.*, **46**, 36-49.

Bankert, R.L., C. Mitrescu, S.D. Miller and R.H. Wade, 2008: Comparison of GOES cloud classification algorithms employing explicit and implicit physics, *Proceedings, 5th GOES Users' Conf.*, Amer. Meteor. Soc., New Orleans, LA, 20-24 Jan 2008.

Byers, H.R. and R.R. Braham, Jr., 1949: *The Thunderstorm*. U.S. Government Printing Office, Wash. D.C., 287 pp.

Cai, H., C. Kessinger, N. Rehak and D. Megenhardt, 2008: Investigation into environmental conditions for storm initiation over the ocean using satellite data, *13th Conf. Aviation, Range, and Aerospace Meteor.,* Amer. Meteor. Soc., New Orleans, LA, 20-24 Jan 2008.

Cummins, K.L., M.J. Murphy, E.A. Bardo, W.L. Hiscox, R.B. Pyle, and A.E. Pifer, A combined TOA/MDF technology upgrade of the U.S. National Lightning Detection Network, J. Geophys. Res., 103, 9035-9044, 1998.

Dixon, M., and G. Wiener, 1993: TITAN: Thunderstorm Identification, tracking, Analysis and Nowcasting - A radar-based methodology. *J. Atmos. Oceanic Technol.,* **10**.,785-797.

Donaldson, R. J., R. M. Dyer, and M. J. Kraus, 1975: An objective evaluation of techniques for predicting severe weather events, *Preprints, Ninth Conf. on Severe Local Storms,* Norman, OK, Amer. Meteor. Soc., 321–326.

Donovan, M., E. Williams, C. Kessinger, G. Blackburn, P. H. Herzegh, R. L. Bankert, S. D. Miller, and F. R. Mosher, 2008: The identification and verification of hazardous convective cells over oceans using visible and infrared satellite observations, *J. Appl. Meteor. Clim.*, **47** (1), 164-184.

FAA, 2008: *FAA Aerospace Forecast, Fiscal years 2008-2025*. U.S. Dept. of Transportation, Federal Aviation Administration, Aviation Policy and Plans. Available online at http://www.faa.gov/data_statistics/aviation/aerospace_forecasts/2008-2025/media/2008%20Forecast%20Document.pdf

Franklin, J. L., 2008: Tropical cyclone report, Hurricane Dean (AL042007). National Hurricane Center, available at http://www.nhc.noaa.gov/2007atlan.shtml.

Jenkins, G.S., A.S. Pratt and A. Heymsfield, Possible linkages between Saharan dust and tropical cyclone rain band generation in the eastern Atlantic during NAMMA-06, Geophys. Res. Lett., 35, L08815, doi:10.1029/2008GL034072, 2008.

Kessinger, Cathy C. Mueller, H. Cai, G. Blackburn, N. Rehak, K. Levesque, B. Hendrickson, S. Carson and D. Megenhardt, 2006: Oceanic convection diagnosis and Nowcasting, *5th International Conf. Meso. Meteo. Typh. (ICMCS)*, East Asia Wea. Res. Assoc., Boulder, CO, 31 Oct – 3 Nov 2006. (see http://www.eol.ucar.edu/icmcs/index.html)

Kessinger, C., H. Cai, N. Rehak, D. Megenhardt, J. Hawkins, R. Bankert and E. Williams, 2008: Oceanic Convection Diagnosis and Nowcasting, *13th Conf. Aviation, Range, and Aerospace Meteor.,* Amer. Meteor. Soc., New Orleans, LA, 20-24 Jan 2008.

Kessinger, C., H. Cai, M. Steiner, N. Rehak, D. Megenhardt, J. Hawkins, R. Bankert and E. Williams, 2007: Oceanic Convective Weather Diagnosis and Nowcasting, *Annual Progress Report*, Submitted for NASA CAN – NNH04ZYO010C and NASA ROSES 2005 - NNH05ZDA001N-DECISION Decision Support through Earth-Sun Science Research Results, 15 Nov 2007. Available from the authors.

Megenhardt, D., C. Mueller, S. Trier, D. Ahijevych, and N. Rehak, 2004: NCWF-2 Probabilistic Nowcasts, *Preprints, 11th Conf. Aviation, Range and Aerospace Meteo. Conf.*, Amer. Meteor. Soc., Hyannis, MA, 4-8 October 2004.

Menzel, W. P., 2001: Cloud tracking with satellite imagery: From the pioneering work of Ted Fujita to the present. *Bull. Amer. Met. Soc.*, **82**, 33-47.

Miller, S., T. Tsui, G. Blackburn, C. Kessinger and P. Herzegh, 2005: Technical description of the cloud top height (CTOP) product, the first component of the Convective Diagnosis Oceanic (CDO) product. Unpublished manuscript available from the author at NRL.

Mosher, F., 2002: Detection of deep convection around the globe. *Preprints, 10th Conf. Aviation, Range, and Aerospace Meteor.*, Amer. Meteor. Soc., Portland, OR, 289-292.

Orville, R.E., G.R. Huffines, J. Nielsen-Gammon, R. Zhang, B. Ely, S. Steiger, S. Phillips, S. Allen, and W. Read, Enhancement of cloud-to-ground lightning activity over Houston, Texas, Geophys. Res. Lett., 28, 2597-2600, 2001.

Pavolonis, M.J. and A.K. Heidinger, 2004: Daytime cloud overlap detection from AVHRR and VIIRS. *J. Appl. Meteor,* **43**, 762-778.

Pavolonis, M.J., A.K. Heidinger, and T. Uttal, 2005: Daytime global cloud typing from AVHRR and VIIRS: Algorithm description, validation, and comparisons. *J. Appl. Meteor.,* **44**, 804-826.

Pinto, J., C. Mueller, S. Weygandt, D. Ahijevych, N. Rehak, and D. Megenhardt, 2006: Fusing observation- and model-based probability forecasts for the short term prediction of convection, *12th Conf. Aviation, Range, and Aerospace Meteor.,* Amer. Meteor. Soc., Atlanta, GA, 30 Jan-2 Feb 2006.

Prospero, J.M., R.T. Nees and M. Uematsu, Deposition rate of particulate and dissolved aluminum derived from Saharan dust in precipitation in Miami, J. Geophys. Res., 92, 14723-14731, 1987.

Prospero, J.M. and P.J. Lamb, African droughts and dust transport to the Caribbean: Climate change implications, Science, 302, 1024-1027, 2003.

Rosenfeld, D., TRMM observed first direct evidence of smoke from forest fires inhibiting rainfall, Geophys. Res. Lett., 26, 3105-3108, 1999.

Rosenfeld, D., A. Khain, B. Lynn and W.L. Woodley, Simulation of hurricane response to suppression of warm rain by sub-micron aerosols, Atmos. Chem. Phys. 7, 3411-3424, 2007.

Sassen, K., P. J. DeMott, J. M. Prospero, and M. R. Poellot. Saharan dust storms and indirect aerosol effects on clouds: CRYSTAL-FACE results. Geophys. Res. Lett., 30, 1633, 10.1029/2003GL017371, 2003.

Shepherd, J.M. and S.J. Burian, Detection of urban-induced rainfall anomalies in a major coastal city, *Earth Interactions* (in press), 2003.

Steiger, S.M., R.E. Orville, and G. Huffines, Cloud-to-ground lightning characteristics over Houston, Texas: 1989-2000, J. Geophys. Res.,107,10.1029/2001JD001142, 2002.

Tag, P. M., R. L. Bankert, and L. R. Brody, 2000: An AVHRR multiple cloud-type classification package, *J. Appl. Meteor.*, **39**, 125–134.

Van den Heever, S.C., G.G. Carrio, W.R. Cotton, P.J. DeMott, and A.J. Prenni, Impacts of nucleating aerosol on Florida convection. Part I: Mesoscale Simulations. J. Atmos. Sci., 63, 1752-1775, 2006.

Wilks, Daniel S., 1995: *Statistical Methods in the Atmospheric Sciences*. Academic Press, San Diego, 467 pp.

Williams, E.R., and Coauthors, 2002: Contrasting convective regimes over the Amazon: Implications for cloud electrification, J. Geophys. Res., LBA Special Issue, 107, D20, 8082, doi:10.1029/2001JD000380, 2002.

Williams, J.K., D.A. Ahijevych, C.J. Kessinger, T.R. Saxen, M. Steiner, and S. Dettling, 2008: A machine learning approach to finding weather regimes and skillful predictor combinations for short-term storm forecasting, *13th Conf. Aviation, Range and Aerospace Meteor. Conf.,* Amer. Meteor. Soc., New Orleans, LA, 21-24 Jan 2008.